Evidences against cuspy dark matter halos in large galaxies

Davi C. Rodrigues,[1][*] Antonino del Popolo[2,3][†] Valerio Marra,[1][‡]
Paulo L. C. de Oliveira,[1][§]

[1]*Departamento de Física, Universidade Federal do Espírito Santo, Av. F.Ferrari, 514, 29075-910, Vitória, Brazil.*
[2]*Dipartamento di Fisica e Astronomia, Università di Catania, Viale Andrea Doria 6, 95125 Catania, Italy.*
[3]*INFN sezione di Catania, Via S. Sofia 64, 95123 Catania, Italy*

ABSTRACT
We develop and apply new techniques in order to uncover galaxy rotation curves (RC) systematics. Considering that an ideal dark matter (DM) profile should yield RCs that have no bias towards any particular radius, we find that the Burkert DM profile satisfies the test, while the Navarro-Frenk-While (NFW) profile has a tendency of better fitting the region between one and two disc scale lengths than the inner disc scale length region. Our sample indicates that this behaviour happens to more than 75% of the galaxies fitted with an NFW halo. Also, this tendency does not weaken by considering "large" galaxies, for instance those with $M_* \gtrsim 10^{10} M_\odot$. Besides the tests on the homogeneity of the fits, we also use a sample of 62 galaxies of diverse types to perform tests on the quality of the overall fit of each galaxy, and to search for correlations with stellar mass, gas mass and the disc scale length. In particular, we find that only 13 galaxies are better fitted by the NFW halo; and that even for the galaxies with $M_* \gtrsim 10^{10} M_\odot$ the Burkert profile either fits as good as, or better than, the NFW profile. This result is relevant since different baryonic effects important for the smaller galaxies, like supernova feedback and dynamical friction from baryonic clumps, indicate that at such large stellar masses the NFW profile should be preferred over the Burkert profile. Hence, our results either suggest a new baryonic effect or a change of the dark matter physics.

Key words: galaxies: spiral, galaxies: kinematics and dynamics, dark matter

1 INTRODUCTION

According to the ΛCDM model, our Universe is mainly composed of non-baryonic matter. This model is very successful in describing the early universe state, the formation and evolution of cosmic structures, and the abundance of the matter-energy content of the Universe (e.g., Das et al. 2011; Hand et al. 2012; Hinshaw et al. 2013; Ade et al. 2016), for reviews see Mo et al. (2010); Del Popolo (2013, 2014). However, it has several issues on small scales (e.g., Moore 1994; Flores & Primack 1994; Gilmore et al. 2007; Primack 2009; de Blok 2010; Weinberg et al. 2013; Pawlowski et al. 2015; Oñorbe et al. 2015), see Del Popolo & Le Delliou (2017) for a recent review.

The most persistent of the quoted problems is the so-called cusp-core problem (Moore 1994; Flores & Primack 1994) concerning the discrepancy between the cuspy profiles obtained in N-body simulations (e.g., the NFW profile,

Navarro et al. 1996a, 1997; Navarro et al. 2010) and the profiles inferred from the observed dwarf and low surface brightness (LSB) galaxies, which show cored profiles.

The N-body dark matter (DM) cosmological simulations find inner DM density profiles of virialized halos sharply increasing towards their centres (the cusp of the DM profiles). In the case of the NFW profile, the inner DM halo slope is $\rho \propto r^{-1}$, while in more recent simulations, or semi-analytical models, the inner slope decreases towards the centre, reaching $\rho \propto r^{-0.8}$ at ~ 100 pc from the centre (Stadel et al. 2009; Navarro et al. 2010; Taylor & Navarro 2001; Del Popolo 2011).[1] To be more precise, we should recall that several authors, considering dark matter only simulations or semi-analytical results, found a correlation between the inner slope and the mass of the object considered (e.g., Ricotti 2003; Ricotti et al. 2007; Del Popolo 2010, 2012b; Di Cintio et al. 2014), such that the inner slope could be either a bit above or below -1, depending on the system mass.

[*] E-mail:davi.rodrigues@cosmo-ufes.org
[†] E-mail:adelpopolo@oact.inaf.it
[‡] E-mail:valerio.marra@cosmo-ufes.org
[§] E-mail:paulo.oliveira@cosmo-ufes.org

[1] This profile is dubbed Einasto profile (see Gao et al. 2008).

Contrary to the simulation results, the profiles of real galaxies, and in particular that of the dwarf and low surface brightness (LSB) galaxies, are usually better described by cored DM profiles (whose density is about constant at the centre), like the pseudo-isothermal or the Burkert profiles (Blais-Ouellette et al. 2001; Borriello & Salucci 2001; de Blok et al. 2001a; de Blok et al. 2001b; Swaters et al. 2003; Gentile et al. 2004; Gentile et al. 2005; Oh et al. 2011). Hence there is a conflict between the DM-only simulation results and the DM profiles that are observationally favoured. This conflict is well known in the context of dwarf and LSB galaxies, which should have a cuspy profile (with slope $\alpha \lesssim -1$) according to DM-only simulations, while observational data favour cored profiles ($\alpha \sim 0$). The previous tendency is not valid for all galaxies. de Blok et al. (2008) found that in the THINGS sample larger galaxies ($M_B < -19$) are described equally well by cuspy (NFW) or cored profiles (pseudo-isothermal), while smaller ones ($M_B > -19$) are better described by the pseudo-isothermal profile.[2]

The situation with the most massive disc galaxies is not so clear, since the inner parts of these galaxies are usually baryon dominated. Nonetheless, Spano et al. (2008) using 36 disc galaxies of diverse types found that only 4 of the 36 galaxies yielded fits that were clearly better with the NFW profile, while 18 yielded fits that were clearly better with the pseudo-isothermal profile. They could not find a morphological trend on a possible preference between the NFW profile or the pseudo-isothermal one. Also, it is suggested that the comparison of χ^2 values limited to the central regions could clarify further their results. In the present work we aim to re-evaluate this issue with a larger sample and new techniques, which also make use of χ^2 analyses limited to the central regions of galaxies.

Apart from considerations on alternative approaches to DM, like self-interacting DM (Spergel & Steinhardt 2000; Rocha et al. 2013), change of the spectrum at small scales (Bode et al. 2001; Zentner & Bullock 2003; Macciò et al. 2013), or modified gravity (e.g., van den Bosch & Dalcanton 2000; Zlosnik et al. 2007; Rodrigues et al. 2010; Famaey & McGaugh 2012; Rodrigues et al. 2014; de Almeida et al. 2016; Sánchez-Salcedo et al. 2016a), different proposals on how to solve this disagreement between simulations and observational data consider that baryonic effects may play a relevant role. Within the latter picture, interactions of baryons with DM through gravity could "heat" the DM component giving rise to flatter inner profiles (Del Popolo 2009; Governato et al. 2010; Del Popolo 2012a; Pontzen & Governato 2012; Governato et al. 2012; Del Popolo et al. 2014).

Independently of the precise dominant baryonic mechanism (which includes supernova feedback, and baryonic clumps with dynamical friction), the transformation from a cusp to a core would depend on the baryonic content of each galaxy, and would be more efficient on some galaxies than in others. All the cited approaches agree that, for the largest galaxies, one should not find a cored profile. In particular, and in accordance with Di Cintio et al. (2014) and

Del Popolo & Pace (2016), this transformation of the central cusp into a core correlates with the galaxy stellar mass (M_*), such that galaxies with $M_* \sim 10^{8.5} M_\odot$ have DM profiles that are close to a cored profile, while the largest galaxies (i.e., those with stellar masses about or above $10^{9.5} M_\odot$) are better described by a cuspy DM halo with central slope about -1, or even lower. This behaviour would be a consequence of the fact that the ratio between stellar mass to halo mass is higher in the largest galaxies and that the central regions of these galaxies are dominated by baryons. The large amount of baryonic matter deepens the Newtonian potential more than what happens in dwarf galaxies and, consequently, the outflows generated by the supernovae, or by the dynamical friction from baryonic clumps, are not able to drag away enough DM and flatten the DM profile.

This work aims to develop new approaches to evaluate galaxy fits, which will be used to re-evaluate the cusp-core issue. Several galaxies of diverse types are considered here, but focus is given to the largest galaxies, since the approaches that indicate that baryonic physics can transform the cusp into a core usually also state that this transformation happens for "small" galaxies, while the same baryonic mechanism cannot remove the cusp for galaxies with $M_* \gtrsim 10^{10} M_\odot$ (e.g., Del Popolo 2009; Governato et al. 2010; de Souza et al. 2011; Inoue & Saitoh 2011; Governato et al. 2012; Di Cintio et al. 2014; Del Popolo & Hiotelis 2014; Tollet et al. 2016; Del Popolo & Pace 2016). Actually, the baryonic physics in such large galaxies is expected to lead to DM profiles whose central slope becomes more negative than -1. Here, we look for possible systematics that could favor, or disfavour, the presence of DM cusps in large galaxies. This is an important issue since it could indicate poor understanding of the baryonic physics, or issues with the standard DM model.

The paper is organized as follows: in the next section we present the technique for evaluating the homogeneity of galaxy RC fits. This technique is based on approaches developed in de Blok & Bosma (2002); Rodrigues et al. (2014). Sections 3 and 4 explain, respectively, the DM profiles and the galaxy samples that are here used. In Section 5 we present our main results, which include the application of the technique introduced in Sec. 2. Section 6 is devoted to our conclusions and discussions, while the Appendices A and B clarify assumptions and results from the Sections 2 and 5, respectively.

2   TESTING THE UNIFORMITY OF FITS AND DATA: THE QUANTITIES ξ, ζ AND $\Delta\xi$

Rodrigues et al. (2014) generalized the approach proposed by de Blok & Bosma (2002), which will be further developed here. Hence, first we will briefly review the quantities $\chi^2_{\rm inn}$ and $\chi^2_{\rm out}$ which were introduced in the latter reference. After the minimum value of χ^2 is found ($\chi^2_{\rm min}$), one considers two quantities, the inner and the outer values of χ^2, and these are denoted by $\chi^2_{\rm inn}$, $\chi^2_{\rm out}$. Let $R_{\rm max}$ be the largest radius of the observational RC. The value of $\chi^2_{\rm inn}$ is found from $\chi^2_{\rm min}$ but considering only the observational data from the galaxy centre to $R_{\rm max}/2$, while $\chi^2_{\rm out}$ considers the radii from $R_{\rm max}/2$ to $R_{\rm max}$. de Blok & Bosma (2002) found that the pseudo-isothermal halo leads to better fits than the NFW

---

[2] Also, there are some observational results that do not favour any universal profile (e.g., Simon et al. 2005), which may be related to the environment and the different ways the galaxies formed (Del Popolo 2012a).

halo for most of the cases of their sample (this step is just a straightforward comparison of $\chi^2_{\min}$). And, by using the quantities χ^2_{inn} and χ^2_{out}, they could point out that the main problem with the NFW fits were clearly in the inner region.

In order to further explore the inner radii dynamics, Rodrigues et al. (2014) consider three reference radii, and these are not based on $R_{\max}$, which is not directly related to the inner dynamics, but to the disc scale length (h). These reference radii lead to the definition of the quantities: $\chi^2_{h/2}$, χ^2_h and χ^2_{2h}. These three quantities are given by $\chi^2_{\min}$ but considering only radii either up to $h/2$, h, or $2h$, respectively.

To introduce a proper notation, we write the quantity χ^2 as

$$\chi^2(p_j) \equiv \sum_{i=1}^{N} \left(\frac{V_{\mathrm{model}}(R_i, p_j) - V_i}{\sigma_i} \right)^2, \qquad (1)$$

where V_i and σ_i are the observed RC velocity and its corresponding error at the radius R_i, N is the number of observational data points of the RC (i.e., $R_N = R_{\max}$), and $V_{\mathrm{model}}(R_i, p_j)$ is the theoretical circular velocity at the radius R_i with the model parameters p_j. Using this notation, the quantity χ^2_h, for example, can be written as,

$$\chi^2_h \equiv \sum_{i=1}^{N(h)} \left(\frac{V_{\mathrm{model}}(R_i, \bar{p}_j) - V_i}{\sigma_i} \right)^2, \qquad (2)$$

where $\bar{p}_j$ are the parameters values that minimize χ^2 (i.e., $\chi^2(\bar{p}_i) = \chi^2_{\min}$). The number $N(h)$ is the largest natural number such that $R_{N(h)} \leq h$. Equivalently, $N(h)$ is the number of RC data points at $0 \leq R \leq h$. Analogous definitions are used for $\chi^2_{h/2}$ and χ^2_{2h}.

In order to evaluate the uniformity of the fits along the galaxy radius, we introduce the quantity

$$\xi(m,n) \equiv \frac{\chi^2_{mh}}{\chi^2_{nh}}, \qquad (3)$$

in a similar way as done by Rodrigues et al. (2014), where m and n are real dimensionless numbers. The quantity χ^2_{mh} is defined as in eq. (2), but with $N(h)$ replaced by $N(mh)$.

For an ideal set of galaxies whose observational data is homogeneously distributed along their radius, and for an ideal model with no bias towards any radius, on average one should find

$$\langle \xi(m,n) \rangle \approx \frac{m}{n}, \qquad (4)$$

where $\langle \ \rangle$ stands for a certain average, which will be detailed afterwards.

It is important to select a suitable average for the problem. Since the quantity $\xi(m,n)$, when applied to real galaxies, sometimes changes by more than one order of magnitude from one galaxy to another, the arithmetic mean becomes easily dominated by a few outliers. Instead of developing an algorithm to define and eliminate the outliers, we simply use – as in Rodrigues et al. (2014) – the median as a robust estimator for the average. Doing so we consider the complete data, without discarding any "outlier". Moreover, Appendix A describes in detail a particular case, in contact with the procedures here used, in which eq. (4) holds exactly if the median is employed. One of the conditions for the latter result is that $m = 2n$, and this relation will be used in Sec. 5. Unless otherwise stated, all the averages in this work are performed using the median.

Apart from notation changes, the framework presented above for testing the homogeneity of galaxy fits was proposed in Rodrigues et al. (2014). In particular it was found that the fits derived from the NFW halo had a tendency of better fitting the region $2h > R > h$ than the region $R < h$. It should be emphasised that this test is not a comparison between two different models, it is a consistent test. It compares the fit yielded by certain model at certain radius to the fit of the same model at a different radius.

Even using the median as the average and a perfect model with no bias towards any galaxy radius, eq. (4) may fail to hold as observational data are not, in general, uniformly distributed and with constant error. In order to quantify the non-uniformity of RC data, we extend the approach of Rodrigues et al. (2014) and introduce here the quantity $\zeta(m,n)$. This quantity is supposed to extend eq. (4) to the case of real galaxies. That is, it should be such that for a model without a significant bias towards any particular radius,

$$\langle \xi(m,n) \rangle \approx \langle \zeta(m,n) \rangle. \qquad (5)$$

If a given RC has constant error bars, then ζ should only depend on the number of data points with radius $R \leq mh$ (i.e., $N(mh)$) and $R \leq nh$ (i.e., $N(nh)$). Hence, in this context a natural definition for ζ would be $\zeta(m,n) = N(mh)/N(nh)$. If the data points are evenly spaced, then $N(mh)/N(nh) = m/n$ and one recovers eq. (4).

Non-constant error bars are another source of non-uniformity along the galaxy radius. Since χ^2 depends on the sum of the inverse of σ_i^2, the following quantity will be useful

$$\Sigma(mh) \equiv \sum_{i=1}^{N(mh)} \frac{1}{\sigma_i^2}. \qquad (6)$$

For a RC whose error bars have the same magnitude, one finds that $\Sigma(mh)/\Sigma(nh) = N(mh)/N(nh)$, thus finding the previous case. This quantity already depends on both the magnitude of the error bars and the number of data points, it is also directly related to the definition of χ^2 and generalizes previous considerations. Hence, considering eq. (5), we define ζ as,

$$\zeta(m,n) \equiv \frac{\Sigma(mh)}{\Sigma(nh)}. \qquad (7)$$

For ideal models without bias towards any radii, one should also expect that the dispersions of ξ and ζ should be similar. To quantify the dispersion we introduce the quantities $\sigma^{\pm}_{50\%}$ and $\sigma^{\pm}_{25\%}$. The first one, applied to some set of numerical data $\{X\}$ whose median value is $\langle X \rangle$, is defined as

$$\sigma^+_{50\%}(X) \ = \ \langle \{X \mid X \geq \langle X \rangle\} \rangle, \qquad (8)$$

$$\sigma^-_{50\%}(X) \ = \ \langle \{X \mid X \leq \langle X \rangle\} \rangle. \qquad (9)$$

In other words, $\sigma^+_{50\%}(X)$ is the median of the subsample of $\{X\}$ composed by the X values that are larger or equal to $\langle X \rangle$.

Since, from the definition of the median, about half of the members of a set $\{X\}$ will be above its median, and half below it, one sees that about half of set $\{X\}$ will be in the range $\sigma^-_{50\%}(X) \leq X \leq \sigma^+_{50\%}(X)$.

The quantity $\sigma_{25\%}^{\pm}$ subdivides further the set $\{X\}$. It fixes a range that includes the median and in which about 25% of the sample elements are present, namely,

$$\sigma_{25\%}^{+}(X) = \langle\{X \mid \sigma_{50\%}^{+}(X) \geq X \geq \langle X \rangle\}\rangle, \quad (10)$$

$$\sigma_{25\%}^{-}(X) = \langle\{X \mid \sigma_{50\%}^{-}(X) \leq X \leq \langle X \rangle\}\rangle. \quad (11)$$

If the sample is sufficiently representative, the above quantities can be probabilistically interpreted in the following ways: i) the probability for a random galaxy to lie inside the region between $\sigma_{k\%}^{-}$ and $\sigma_{k\%}^{+}$ is $k\%$; ii) The probability of finding a member of the sample X that is above the corresponding $\sigma_{50\%}^{+}(X)$ is 25%.; iii) and thus the probability of finding an element X that is below $\sigma_{50\%}^{+}(X)$ is 75%.

At last, to further clarify and simplify the analysis, we also introduce the quantity

$$\Delta\xi(m,n) \equiv \xi(m,n) - \zeta(m,n), \quad (12)$$

whose average, for an ideal model, should yield,

$$\langle\Delta\xi(m,n)\rangle \approx 0. \quad (13)$$

For an arbitrary sample of data neither eq. (13) implies eq. (5) nor the contrary, but both are expected to hold if the sample is sufficiently large.

3   DARK MATTER PROFILES

As said in the Introduction, there are different approaches that try to solve the cusp-core problem by flattening the central DM profile of dwarf and LSB galaxies. These mechanisms are not expected to alter the cuspy DM profile of the largest disc galaxies. It is the purpose of this work to use traditional tests in order to compare different DM halo proposals and, also, to apply the methodology presented in the previous section. The main motivation is to look for new evidences against or in favor of the existence of cusps in the DM profiles of the large galaxies.

We consider here two DM profiles that only differ on their behaviour close to the galactic centre, the Navarro-Frenk-White (NFW) profile (Navarro et al. 1996b; Navarro et al. 1997; Navarro et al. 2010),

$$\rho_{\mathrm{NFW}}(r) = \frac{\rho_s}{\frac{r}{r_s}\left(1 + \frac{r}{r_s}\right)^2}, \quad (14)$$

which depends on two parameters, r_s and ρ_s, and the Burkert profile (Burkert 1995),

$$\rho_{\mathrm{B}}(r) = \frac{\rho_c}{\left(1 + \frac{r}{r_c}\right)\left(1 + \frac{r^2}{r_c^2}\right)}, \quad (15)$$

which also depends on two parameters, r_c (the core radius) and ρ_c.

The Burkert profile is a cored profile that is well known for its phenomenological success[3] (e.g., Gentile et al. 2005; Gentile et al. 2004, 2007; Salucci et al. 2007), and it is such that for small radii it has a constant density, and for large radii it decays just like the NFW profile, that is, with r^{-3}.

---

[3] Another well known cored profile is the pseudo-isothermal profile (Begeman et al. 1991), nonetheless this profile differs from the NFW one at both small and large radius.

Table 1. The five data samples considered in Rodrigues et al. (2014). Unless otherwise stated, we refer to different baryonic models as different galaxies. There are different ways of removing these repetitions, but neither has lead to significant systematic effects that could change any of the conclusions.

Sample	Fitted galaxies	Main Refs.
A	18	de Blok et al. (2008)
B	05	Gentile et al. (2004)
C	13	de Blok & Bosma (2002)
D	08	de Blok et al. (2001a)
E	18	Swaters et al. (2011)
Total	62 different baryonic models for galaxies	
	53 different galaxies	

According to Di Cintio et al. (2014); Del Popolo & Pace (2016); Tollet et al. (2016), galaxies with stellar to DM mass ratio $M_*/M_{\mathrm{DM}} \gtrsim 10^{-1.7}$ (or, equivalently, using the Moster et al. (2013) relation, $M_* \gtrsim 10^{9.5}M_{\odot}$) have inner slope $\alpha \leq -0.6$; while for $M_*/M_{\mathrm{DM}} \gtrsim 10^{-1.5}$ (or $M_* \gtrsim 10^{10.0}M_{\odot}$) the inner slope is $\alpha \leq -1.0$. Since the NFW and Burkert profiles' inner slopes are respectively -1 and 0, while their outer slopes are both -3, it is expected that for galaxies with stellar mass about or above $10^{9.5}M_{\odot}$ one should find that the NFW halo leads to better fits than the Burkert halo.

Although the NFW profile, as defined in eq. (14), depends on two parameters, several simulations assert that there is a correlation between these parameters (the correlation is usually parameterised with the concentration c and M_{200}) (e.g., Macció et al. 2008). Some works use this correlation to write one parameter as a function of the other (e.g., Gentile et al. 2005), thus arriving on a one-parameter NFW halo. Since there is significant dispersion on such correlations (including differences between different works), here both the parameters are fitted without constraints, which implies that the NFW results used in this work are the best possible fits with this profile.

The present work uses the (two-parameter) NFW fits from Rodrigues et al. (2014), where further details (including the correlation between c and M_{200} from the observational data) can be found. For the Burkert fits, all the fits are done here and constitute part of the results of this work. Some of the galaxies that we consider here were previously fitted with the Burkert profile; nonetheless, to assure uniformity on all the conventions, we fitted all the galaxies with the Burkert profile using precisely the same procedures that we used for the NFW fits.

4   SAMPLES

Table 1 lists the five galaxy data samples that were studied in Rodrigues et al. (2014) and their corresponding main references. We refer to the latter reference for a table with the galaxy global parameters (including luminosity, distance and disc scale length).

The complete sample contains precisely 53 different galaxies and 62 different baryonic models for galaxies. For instance, in the Sample A two different models for the galaxy NGC 3198 can be found (one with a bulge and the other without), and the galaxy F 563-1 can be found in both the samples C and D. We do not try to advocate which of these

Table 2. The samples and the corresponding number of galaxies that have one or more RC data points at $R < h/2$, $R < h$, and $R < 2h$. These are respectively denoted by $N_G(h/2)$, $N_G(h)$, and $N_G(2h)$. The samples $\mathcal{S}_{*1}$ and $\mathcal{S}_{*2}$ are the only ones whose number of members is model dependent, hence their N_G values are stated in the form NFW/Burkert. Below, M_* is the total stellar mass (bulge and disc), h is the disc scale length and M_{gas} is the gas mass (it includes hydrogen and helium contributions, and follows the prescriptions from the corresponding original reference).

Sample	Sample criterion	$N_G(h/2)$	$N_G(h)$	$N_G(2h)$
A	-	14	17	18
B	-	5	5	5
C	-	13	13	13
D	-	7	8	8
E	-	12	18	18
$\mathcal{S}$	All galaxies	51	61	62
$\mathcal{S}_{*1}$	$M_* > 10^9 M_\odot$	29/32	34/39	35/40
$\mathcal{S}_{*2}$	$M_* > 10^{10} M_\odot$	13/12	16/16	17/17
$\mathcal{S}_{g1}$	$M_{gas} > 10^9 M_\odot$	39	48	49
$\mathcal{S}_{g2}$	$M_{gas} > 5 \times 10^9 M_\odot$	14	17	18
$\mathcal{S}_{h1}$	$h > 1.5$ kpc	42	47	48
$\mathcal{S}_{h2}$	$h > 3.0$ kpc	17	19	19

baryonic models is to be preferred, and we use all the 62 galaxy data. There are different strategies to eliminate duplicate galaxies, some of them were explicitly tested and neither has lead to significant systematic effects that could change our conclusions (which is in part expected since the median is a robust type of average).

The Total Sample ($\mathcal{S}$) is composed by the union of the samples A, B, C, D and E. The subsamples of $\mathcal{S}$ composed by all the galaxies with stellar mass (bulge plus disc stellar masses) above $10^9 M_\odot$ or $10^{10} M_\odot$ constitute respectively the samples named $\mathcal{S}_{*1}$ and $\mathcal{S}_{*2}$. The subsamples of $\mathcal{S}$ composed by all the galaxies with gas mass above $10^9 M_\odot$ or $5 \times 10^9 M_\odot$ constitute respectively the samples named $\mathcal{S}_{g1}$ and $\mathcal{S}_{g2}$. The subsamples of $\mathcal{S}$ composed by all the galaxies with disc scale length above 1.5 kpc or 3.0 kpc constitute respectively the samples named $\mathcal{S}_{h1}$ and $\mathcal{S}_{h2}$. Further details on these samples are shown in Table 2.

Table 3 shows the values of $N(nh)$ and $\Sigma(nh)$ for each of the galaxies.

The galaxy samples used here are well known and used as part of several different tests (e.g., for some recent examples, see Rodrigues et al. 2014; Saburova & Del Popolo 2014; Oman et al. 2015; Sanchez-Salcedo et al. 2016b; Oman et al. 2016; de Almeida et al. 2016; Tollet et al. 2016; Karukes & Salucci 2017). Sample A (de Blok et al. 2008) is the original THINGS sample that includes large and massive spirals, its 21 cm data was presented in Walter et al. (2008) and it uses different infrared bands for modeling the stellar part, including 3.6 μm from Spitzer. Sample B (Gentile et al. 2004) is a small sample of galaxies with dynamical masses from $\sim 10^{10} M_\odot$ to $\sim 10^{11} M_\odot$ that was carefully modeled to study the core-cusp issue with combined HI and Hα data, it uses the infrared I-band to model the stellar part. Samples C (de Blok & Bosma 2002) and D (de Blok et al. 2001a) are classic references on LSB galaxies and on the cusp-core problem. The Sample E (Swaters et al. 2011) is a sample
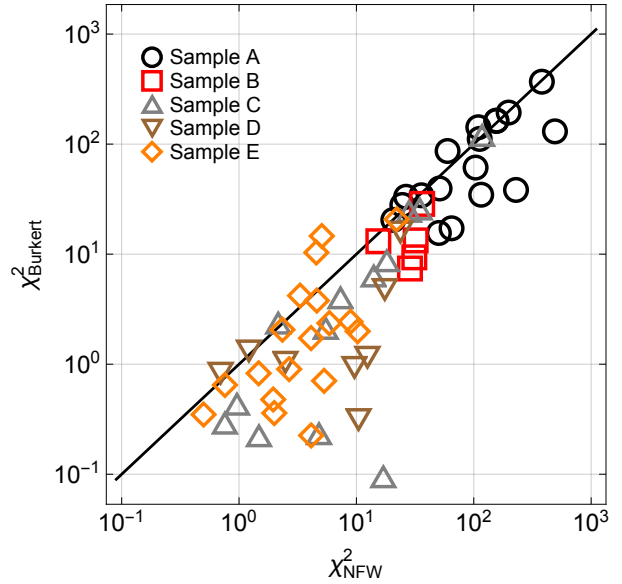
Figure 1. Comparison between the Burkert and the NFW fits considering the minimum χ^2 (which are respectively denoted by $\chi^2_{Burkert}$ and χ^2_{NFW}). The black line is the the straight line where $\chi^2_{NFW} = \chi^2_{Burkert}$. Among our sample of 62 galaxies, only 13 are fitted better with the NFW dark matter halo than with the Burkert one (i.e., they satisfy $\chi^2_{NFW} < \chi^2_{Burkert}$).

with dwarf and LSB galaxies whose RC were derived from both HI and Hα observations. This sample is a selection of the 18 highest quality RC data from the 62 galaxies of Swaters et al. (2009).

Recently, a new large catalogue on 175 disc galaxies was compiled, the SPARC sample (Lelli et al. 2016a). There is a significant intersection between the galaxies of that catalogue and the galaxies that are used in this work, namely, there are 10 galaxies from the SPARC sample that also appear in Sample A, 4 galaxies from Sample B, 4 from Sample C, 3 from Sample D, and 8 from Sample E. On the other hand, there is also a significant amount of galaxies that appear in the latter five samples and do not appear in SPARC. The differences between the galaxy data and baryonic models that appear in more then one sample is commonly small, and some features are identical (e.g., most of the RC data are identical). Among the differences, perhaps unexpectedly, some galaxies that are part of the THINGS sample appear in SPARC, but with RC data from older references. The reason for this choice is detailed in Lelli et al. (2016a). The most relevant difference comes from the indication that all the galaxies may share a fixed stellar mass-to-light ratio (Υ_*) at the 3.6 μm wave length. In this work we do not consider the latter as a starting point, we follow one of the standard approaches to the subject, and find Υ_* for each galaxy from a best fit. In the Appendix C this issue is discussed in detail, and our results on Υ_* are compared to the expectations posed by Lelli et al. (2016a).

5   RESULTS

Our results can be grouped as follows:

Table 3. Values of N and Σ for all the galaxies. These figures are directly derived from the observational data, and hence are model independent.

S	Galaxy	$N(h/2)$	$N(h)$	$N(2h)$	$N(R_{\max})$	$\Sigma(h/2)$	$\Sigma(h)$	$\Sigma(2h)$	$\Sigma(R_{\max})$
A	DDO 154	3	7	14	60	1.85	2.56	4.19	17.36
A	NGC 2403 1D	14	28	57	287	0.53	1.10	2.17	16.25
A	NGC 2403 2D	14	28	57	287	0.53	1.10	2.17	16.25
A	NGC 2841	0	2	14	140	0.00	0.02	0.49	2.71
A	NGC 2903	0	0	6	86	0.00	0.00	0.10	2.91
A	NGC 2976	13	27	42	41	2.28	3.53	4.63	4.55
A	NGC 3031	0	5	31	116	0.00	0.20	2.23	4.16
A	NGC 3198 1D	3	7	15	93	0.08	0.18	0.48	5.31
A	NGC 3198 2D	3	7	15	93	0.08	0.18	0.48	5.31
A	NGC 3521	20	41	83	99	0.61	0.92	1.00	1.06
A	NGC 3621	6	12	24	122	0.39	0.74	1.88	8.11
A	NGC 4736	5	14	31	81	0.16	0.43	1.01	2.76
A	NGC 5055	4	9	19	198	0.05	0.27	0.89	4.66
A	NGC 6946	2	19	54	206	0.10	0.44	1.64	5.86
A	NGC 7331	0	12	38	104	0.00	0.17	0.44	1.41
A	NGC 7793	7	14	28	67	1.27	2.65	3.96	6.22
A	NGC 7793 R	7	14	28	41	1.27	2.65	3.96	4.87
A	NGC 925	8	18	38	95	0.19	0.81	1.52	3.16
B	ESO 116-G12	1	3	5	14	0.08	0.27	0.48	1.82
B	ESO 287-G13	3	6	12	25	0.12	0.34	0.61	2.11
B	ESO 79-G14	3	5	9	14	0.03	0.10	0.21	0.94
B	NGC 1090	3	3	6	23	0.08	0.08	0.21	2.14
B	NGC 7339	2	4	9	14	0.09	0.17	0.86	1.40
C	F 563-1	2	3	3	7	0.01	0.02	0.02	0.08
C	UGC 1230	2	3	6	10	0.02	0.03	0.05	0.08
C	UGC 3060	7	14	29	58	1.75	3.50	7.25	19.43
C	UGC 3371	3	7	12	17	0.03	0.06	0.09	0.24
C	UGC 3851	8	15	18	27	0.31	0.60	0.64	1.02
C	UGC 4173	3	6	10	12	0.06	0.12	0.23	0.28
C	UGC 4325	3	5	11	15	0.04	0.09	0.23	0.26
. C	UGC 5005	1	3	6	10	0.02	0.02	0.07	0.10
C	UGC 5721	1	3	5	22	0.05	0.12	0.20	0.97
C	UGC 7524	11	23	41	54	0.30	0.57	1.05	1.47
C	UGC 7603	2	4	7	19	0.12	0.24	0.42	1.14
C	UGC 8837	3	3	8	7	0.18	0.18	0.43	0.39
C	UGC 9211	1	2	4	10	0.02	0.03	0.05	0.19
D	F 563-1	0	1	2	9	0.00	0.00	0.00	0.05
D	F 568-3	3	5	8	10	0.07	0.10	0.16	0.19
D	F 571-8	3	4	9	12	0.15	0.21	0.39	0.57
D	F 579-V1	3	6	11	13	0.03	0.06	0.10	0.12
D	F 583-1	2	5	9	16	0.03	0.08	0.22	0.36
D	F 583-4	3	3	6	8	0.12	0.12	0.25	0.33
D	UGC 5750	2	4	7	10	0.06	0.08	0.23	0.25
D	UGC 6614	3	3	9	14	0.03	0.03	0.10	0.13
E	UGC 11707	1	3	7	12	0.01	0.05	0.51	1.09
E	UGC 12060	0	1	3	8	0.00	0.05	0.15	0.41
E	UGC 12632	2	5	10	16	0.06	0.38	0.81	1.54
E	UGC 12732	1	2	4	15	0.09	0.14	0.24	1.17
E	UGC 3371	1	3	6	10	0.09	0.36	0.75	1.20
E	UGC 4325	1	2	4	7	0.11	0.21	0.43	0.75
E	UGC 4499	0	1	3	8	0.00	0.06	0.28	0.94
E	UGC 5414	1	2	4	5	0.16	0.33	0.66	0.83
E	UGC 6446	1	2	4	10	0.14	0.30	0.60	1.49
E	UGC 731	1	2	5	11	0.18	0.35	0.67	1.53
E	UGC 7323	1	3	7	9	0.07	0.20	0.47	0.60
E	UGC 7399	0	1	2	17	0.00	0.13	0.22	2.22
E	UGC 7524	5	10	20	30	0.44	1.05	1.71	2.68
E	UGC 7559	1	2	5	8	0.10	0.19	0.48	0.76
E	UGC 7577	1	3	6	8	0.10	0.30	0.60	0.79
E	UGC 7603	0	1	3	11	0.00	0.12	0.36	1.32
E	UGC 8490	0	1	3	29	0.00	0.07	0.22	2.13
E	UGC 9211	0	1	2	8	0.00	0.06	0.12	0.48

Table 4. Best-fit results for our sample of 62 galaxies using the Burkert dark matter profile. This table extends Table 4 of Rodrigues et al. (2014). Col. (1): sample. Col. (3): minimum χ^2. Col. (4): reduced χ^2. Cols. (5)-(7): see Sec. 2 for their definitions. Cols. (8)-(9): disc and bulge stellar mass-to-light ratios in the appropriate band for each sample. Col. (10): r_c (kpc). An "∞" means that the resulting r_c from the fits is larger than 1 Mpc. Col. (11): ρ_c ($M_\odot$/kpc^3).

S	Galaxy	χ^2_{min}	χ^2_{red}	χ^2_{2h}	χ^2_h	$\chi^2_{h/2}$	Υ_{*D}	Υ_{*B}	r_c	ρ_c
(1)	(2)	(3)	(4)	(5)	(6)	(7)	(8)	(9)	(10)	(11)
A	DDO 154	15.58	0.27	2.96	2.52	1.80	3.45	—	4.31	1.03×10^7
A	NGC 2403 1D	163.77	0.58	35.22	13.37	9.10	0.68	—	7.24	2.55×10^7
A	NGC 2403 2D	162.18	0.57	26.52	12.96	9.59	0.59	1.07	6.82	2.87×10^7
A	NGC 2841	33.23	0.24	6.38	2.09	0.00	0.96	1.58	13.91	2.53×10^7
A	NGC 2903	20.47	0.25	0.18	0.00	0.00	1.63	2.45	6.80	4.78×10^7
A	NGC 2976	17.18	0.44	17.18	11.61	9.30	0.25	—	2.38	1.10×10^8
A	NGC 3031	369.14	3.27	113.27	8.46	0.00	0.92	0.26	5.03	2.83×10^7
A	NGC 3198 1D	34.69	0.38	2.93	0.60	0.36	0.12	—	4.34	9.74×10^7
A	NGC 3198 2D	34.27	0.38	2.80	0.30	0.15	0.07	0.08	4.21	1.06×10^8
A	NGC 3521	130.60	1.35	127.22	114.23	113.70	0.00	—	2.14	1.01×10^9
A	NGC 3621	86.59	0.72	23.46	11.92	8.55	0.61	—	12.04	1.05×10^7
A	NGC 4736	111.52	1.43	61.81	19.91	3.19	0.41	0.33	0.84	9.83×10^8
A	NGC 5055	142.33	0.73	71.64	15.15	4.41	0.50	0.38	13.71	1.04×10^7
A	NGC 6946	193.55	0.95	85.30	23.86	12.70	0.61	0.68	16.91	1.02×10^7
A	NGC 7331	27.99	0.28	8.46	4.93	0.00	0.56	0.68	18.20	8.75×10^6
A	NGC 7793	38.33	1.01	33.97	12.85	10.53	0.45	—	∞	2.50×10^7
A	NGC 7793 R	39.52	1.04	34.68	17.36	15.89	0.44	—	∞	2.54×10^7
A	NGC 925	61.22	0.66	28.66	22.98	19.59	0.15	—	8.46	1.61×10^7
B	ESO 116-G12	9.36	0.78	4.08	3.73	2.57	0.43	—	4.39	4.65×10^7
B	ESO 287-G13	28.64	1.25	22.34	17.35	15.98	1.96	—	27.59	4.54×10^6
B	ESO 79-G14	7.40	0.62	5.04	4.26	1.45	0.75	—	7.96	3.45×10^7
B	NGC 1090	13.34	0.64	6.33	0.41	0.41	1.47	—	8.97	1.85×10^7
B	NGC 7339	13.11	1.09	6.35	3.90	0.32	1.82	—	5.54	5.42×10^7
C	F563-1	2.36	0.47	2.28	2.28	0.84	8.48	—	19.59	3.53×10^6
C	UGC 1230	2.11	0.26	1.80	0.94	0.80	0.00	—	3.53	7.77×10^7
C	UGC 3060	119.63	2.14	76.22	42.79	14.66	4.25	—	13.47	6.66×10^6
C	UGC 3371	0.23	0.02	0.13	0.12	0.11	0.00	—	5.55	2.08×10^7
C	UGC 3851	25.68	1.03	24.67	24.50	9.53	0.00	—	1.06	1.73×10^8
C	UGC 4173	0.43	0.04	0.40	0.31	0.18	0.00	—	4.12	8.88×10^6
C	UGC 4325	0.10	0.01	0.08	0.03	0.02	0.46	—	4.32	1.04×10^8
C	UGC 5005	0.22	0.03	0.17	0.12	0.00	2.56	—	11.66	5.31×10^6
C	UGC 5721	8.70	0.44	1.88	0.76	0.10	1.99	—	1.24	3.07×10^8
C	UGC 7524	24.47	0.47	22.07	8.18	4.45	6.67	—	0.68	1.67×10^8
C	UGC 7603	4.01	0.24	0.70	0.45	0.21	1.28	—	3.57	2.81×10^7
C	UGC 8837	6.32	1.26	6.32	0.60	0.60	0.00	—	∞	1.91×10^7
C	UGC 9211	0.29	0.04	0.20	0.16	0.15	0.00	—	1.74	1.00×10^8
D	F563-1	0.83	0.12	0.64	0.22	0.00	10.46	—	16.23	3.50×10^6
D	F568-3	4.78	0.60	4.23	2.29	2.14	0.00	—	4.42	4.36×10^7
D	F578-1	1.16	0.13	1.05	0.53	0.34	0.00	0.46	5.30	6.42×10^7
D	F579-V1	1.04	0.10	0.38	0.15	0.13	5.01	—	0.93	6.40×10^8
D	F583-1	0.31	0.02	0.17	0.10	0.02	0.00	—	3.77	3.87×10^7
D	F583-4	1.32	0.22	0.62	0.27	0.27	9.84	—	0.42	1.14×10^8
D	UGC 5750	0.94	0.12	0.50	0.35	0.24	0.00	—	6.73	1.15×10^7
D	UGC 6614	15.91	1.45	15.82	14.84	14.84	0.01	2.48	12.96	1.87×10^7
E	UGC 11707	10.35	1.04	3.28	0.67	0.19	9.24	—	∞	6.92×10^5
E	UGC 12060	0.35	0.06	0.11	0.04	0.00	7.74	—	23.55	1.08×10^6
E	UGC 12632	14.60	1.04	8.66	6.10	1.72	14.08	—	∞	1.17×10^6
E	UGC 12732	2.06	0.16	0.44	0.11	0.08	6.14	—	12.51	4.24×10^6
E	UGC 3371	3.79	0.47	1.45	0.81	0.58	10.04	—	10.76	3.87×10^6
E	UGC 4325	2.36	0.47	2.10	0.91	0.90	0.16	—	1.45	3.09×10^8
E	UGC 4499	0.71	0.12	0.20	0.01	0.00	0.00	—	2.52	5.91×10^7
E	UGC 5414	0.48	0.16	0.36	0.25	0.11	2.76	—	5.51	9.17×10^6
E	UGC 6446	1.73	0.22	0.92	0.80	0.51	3.21	—	4.53	1.53×10^7
E	UGC 731	0.83	0.09	0.47	0.22	0.01	12.59	—	5.86	6.87×10^6
E	UGC 7323	0.90	0.13	0.85	0.43	0.27	1.96	—	6.91	1.30×10^7
E	UGC 7399	20.72	1.38	2.30	2.02	0.00	6.11	—	3.97	5.20×10^7
E	UGC 7524	2.43	0.09	0.85	0.39	0.29	4.72	—	3.59	1.87×10^7
E	UGC 7559	0.36	0.06	0.27	0.06	0.00	0.00	—	0.88	1.06×10^8
E	UGC 7577	0.65	0.11	0.47	0.29	0.02	0.40	—	∞	8.25×10^5
E	UGC 7603	1.99	0.22	0.41	0.04	0.00	0.66	—	1.94	7.83×10^7
E	UGC 8490	4.20	0.16	2.69	1.41	0.00	3.63	—	2.88	5.07×10^7
E	UGC 9211	0.23	0.04	0.02	0.01	0.00	2.53	—	2.36	5.19×10^7

Table 5. The medians of the quantities $\chi^2_{\rm red}$, χ^2, $\chi^2_{\rm 2h}$, $\chi^2_{\rm h}$ and $\chi^2_{\rm h/2}$. For all of these quantities, and for all the samples and subsamples, the Burkert profile yields lower median results than the NFW profile.

S	Model	$\langle\chi^2_{\rm red}\rangle$	$\langle\chi^2\rangle$	$\langle\chi^2_{2h}\rangle$	$\langle\chi^2_h\rangle$	$\langle\chi^2_{h/2}\rangle$
(1)	(2)	(3)	(4)	(5)	(6)	(7)
A	Burkert	0.62	50.37	27.59	12.85	9.20
	NFW	0.92	106.45	43.89	22.69	16.55
B	Burkert	0.78	13.11	6.32	3.90	1.45
	NFW	1.58	31.15	21.18	13.39	3.11
C	Burkert	0.26	2.36	1.80	0.60	0.21
	NFW	0.54	7.32	5.35	3.45	1.89
D	Burkert	0.12	1.10	0.63	0.31	0.27
	NFW	0.97	10.03	6.73	5.24	2.57
E	Burkert	0.16	1.86	0.66	0.34	0.23
	NFW	0.42	4.11	2.00	1.37	0.61
$\mathcal{S}$	Burkert	0.38	6.86	2.50	0.81	0.58
	NFW	0.67	14.72	6.11	4.42	2.93
$\mathcal{S}_{*1}$	Burkert	0.47	14.60	4.08	2.18	0.84
	NFW	0.71	22.87	10.69	6.64	4.18
$\mathcal{S}_{*2}$	Burkert	0.73	24.23	7.42	4.93	1.72
	NFW	1.27	31.97	21.18	10.41	7.91
$\mathcal{S}_{\rm g1}$	Burkert	0.47	10.35	2.93	1.71	0.90
	NFW	0.68	20.64	7.51	6.05	4.08
$\mathcal{S}_{\rm g2}$	Burkert	0.43	28.31	6.35	2.28	2.62
	NFW	0.62	29.24	13.85	8.29	7.35
$\mathcal{S}_{\rm h1}$	Burkert	0.47	11.73	3.68	2.09	0.82
	NFW	0.57	19.04	7.80	5.94	3.19
$\mathcal{S}_{\rm h2}$	Burkert	0.38	7.40	2.93	0.81	0.41
	NFW	0.57	17.44	7.51	4.42	4.24

1) Burkert fits of individual galaxies, see Table 4.
2) Analyses of the χ^2 values for each galaxy, comparing Burkert and NFW profiles. See Figs. 1-2.
3) Medians of the quantities χ^2, $\chi^2_{\rm red}$ and χ^2_{mh}, see Table 5.
4) Analyses of the quantities ξ, ζ and $\Delta\xi$. Fig. 3 summarizes the detailed results shown in Appendix B.

Figure 1 compares the minimum χ^2 derived from the Burkert and NFW profiles. There is a clear preference for the Burkert profile since among our sample of 62 galaxies only 13 have better fits when using the NFW profile. Moreover, those that are better fitted with the NFW profile only slightly favor the latter.

Figure 1 also shows that some samples have larger χ^2 values than others. This is expected since the χ^2 values depend on the number of RC data points, and the latter depend on both the angular resolution of the 21 cm data and on the size and distance of the observed galaxies. For example, Sample A includes several large nearby galaxies and features 21 cm observations with the highest angular resolution, thus it is expected to yield the highest values for χ^2. For the reduced χ^2 results of Sample A, one can see from Table 5 that there is no discrepancy in regard to other samples.

Figure 2 shows plots whose purpose is to analyse correlations between the fraction $\chi^2_{\rm NFW}/\chi^2_{\rm Burkert}$ and certain galaxy parameters, namely: the stellar mass, gas mass and the final circular velocity V_f. It is not shown but correlations with the disc scale length were also tested, and they lead to qualitatively similar results, but with a dispersion about the same or higher. It can be noted from the upper plots of Fig. 2 that the values of $\chi^2_{\rm NFW}/\chi^2_{\rm Burkert}$ have larger dispersion at about $M_* \sim 10^8 M_\odot$ or $M_* \sim 10^9 M_\odot$, and that the dispersion decreases and the fraction $\chi^2_{\rm NFW}/\chi^2_{\rm Burkert}$ ap-

proaches 1 as one considers larger stellar masses. It was not possible to find that galaxies with $10^{9.5}M_\odot$ or higher stellar masses favor the NFW profile (i.e., $\chi^2_{\rm Burkert} > \chi^2_{\rm NFW}$).[4] The analyses with the disc scale length (h) and the gas mass lead to similar results, but with a less clear correlation related to the fraction $\chi^2_{\rm NFW}/\chi^2_{\rm Burkert}$.

In Table 5, medians of χ^2-related quantities are displayed for the various samples. For all the samples, even those that select the largest galaxies (i.e., $\mathcal{S}_{*2}$, $\mathcal{S}_{g2}$ and $\mathcal{S}_{h2}$), all the χ^2-related quantities have lower values when the dark matter halo profile is the Burkert one.[5]

We now discuss our results regarding the quantities ξ, ζ and $\Delta\xi$. With the values of $\chi^2_{\rm h/2}$, $\chi^2_{\rm h}$ and $\chi^2_{\rm 2h}$ for each galaxy, essentially two different ξ quantities, as introduced in Sec. 2, can be evaluated: $\xi(1, 1/2)$ and $\xi(2, 1)$. The quantity $\xi(2, 1/2)$ is a combination of the previous two. Considering the median results for the sample $\mathcal{S}$, the upper plot of Fig. 3 shows that both the profiles have about the same behaviour, and both display a tendency to better fit the region $h/2 < R < h$ than the region $0 < R < h/2$.[6] Considering

---

[4] We have included the bulge in our analyses, but no significative change is observed if the bulge is not considered.

[5] Some care is necessary on the issue of $\chi^2_{\rm red}$, since a large fraction of the found values have very low values of $\chi^2_{\rm red}$. Supposing that the error bars of all galaxies were properly evaluated, one is to expect that $\langle\chi^2_{\rm red}\rangle \approx 1$. To properly consider all the diverse systematical errors in external galaxies is not an easy task, and a reliable and feasible procedure is probably currently unknown. Likewise in many other papers on the subject (e.g., de Blok & Bosma 2002; de Blok et al. 2008; Gentile et al. 2011) we use χ^2 or $\chi^2_{\rm red}$ to compare fits relative to different models and not to obtain an absolute goodness-of-fit.

[6] The fits are on average about 25% better in the region $h/2 <$
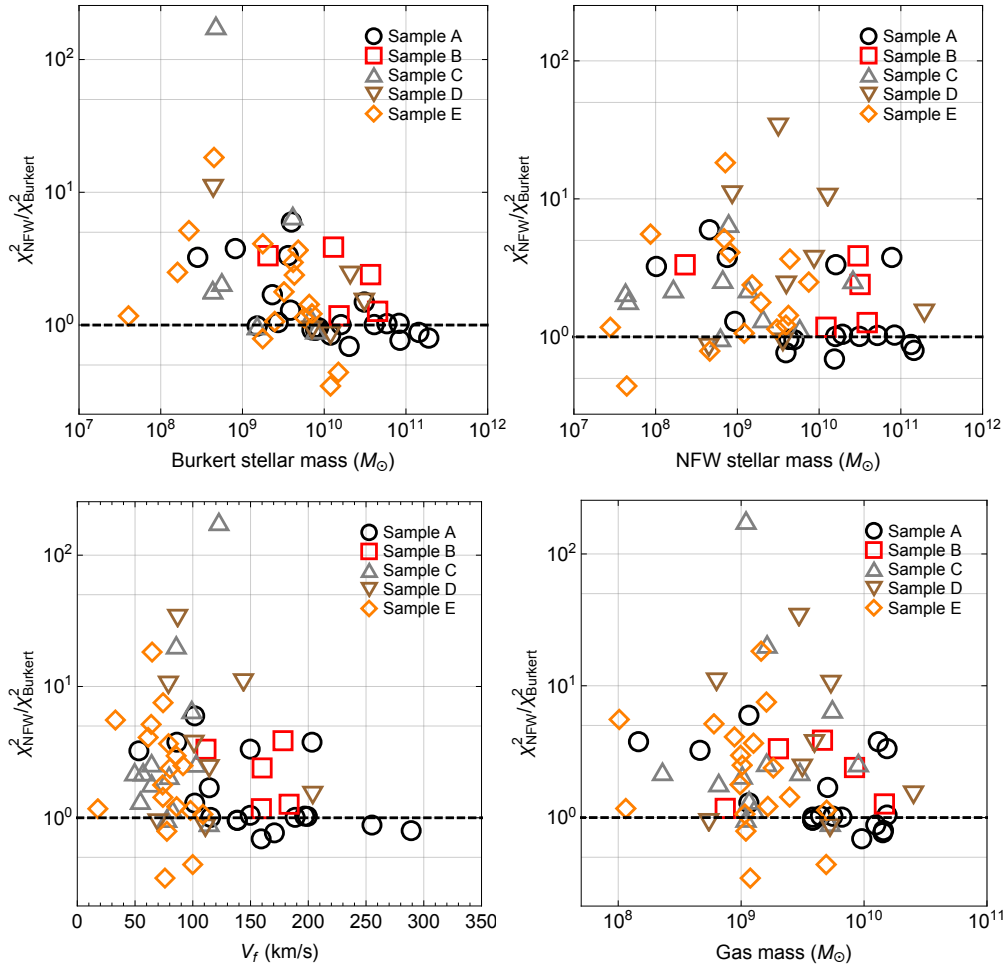
Figure 2. Each plot shows the relation between the ratio $\chi^2_{\mathrm{NFW}}/\chi^2_{\mathrm{Burkert}}$ and the following parameters: i) (top left) the total stellar mass (disc and bulge) derived from the fits that use the Burkert profile, ii) (top right) same as the previous case, but using the NFW profile, iii) (bottom left) the final velocity V_f (see Appendix C for further details), and iv) (bottom right) the total gas mass. The first two plots show a trend such that, for galaxies with stellar mass above $\sim 10^{9.5} M_\odot$, the higher is the stellar mass the lower is the dispersion on the plane $\chi^2_{\mathrm{NFW}}/\chi^2_{\mathrm{Burkert}} \times M_*$, and the closer the data are to $\chi^2_{\mathrm{NFW}}/\chi^2_{\mathrm{Burkert}} \sim 1$. Qualitatively similar trends can also be seen in the other plots above.

the inferred dispersions, one sees that the expected value of $\langle \Delta \xi(1, 1/2) \rangle$, which is zero, is close to the upper limit of $\sigma_{25\%}$ (i.e., $\sigma^+_{25\%}$) for both of the profiles.[7] One sees, from considering only the largest galaxies (i.e., the other six samples), that the above "tension" has a small tendency to increase. In case further analyses confirm and enlarge this tension for both of the profiles, a possible interpretation is that a systematic issue with the central part of the stellar profiles is being uncovered, see also Sec. 6. In particular, it may be related to disc and bulge decomposition issues, non-circular motions or differential dust opacity (see e.g., Courteau et al. 2014).

The results associated to $\langle \Delta \xi(2, 1) \rangle$ display stronger differences between the profile results. As it can be seen in the

bottom plot of Fig. 3, the $\mathcal{S}$ sample results indicate the existence of a good agreement between the Burkert value of $\langle \Delta \xi(2, 1) \rangle$ and the expected value of zero. The expected value is clearly well inside the $\sigma_{25\%}$ error bars of the Burkert profile. On the other hand, for the NFW profile results, the expected value is outside the $\sigma_{50\%}$ error bars, hence more than 75% of the galaxies fitted with NFW are in tension with a homogeneous fit.[8]

Considering the sample $\mathcal{S}$ results, the plot at the bottom of Fig. 3 shows that the Burkert profile provides RC fits that are homogeneous with respect to the regions $0 < R < h$ and $h < R < 2h$, while the NFW profile has a clear tension with homogeneity, fitting on average the region $h < R < 2h$ better than the region $0 < R < h$. Upon considering the six subsamples that select the largest galaxies, both the models lead essentially to the same results, with a small tendency towards more negative $\langle \Delta \xi(2, 1) \rangle$ values for the three most restrictive subsamples ($\mathcal{S}_{*2}$, $\mathcal{S}_{g2}$ and $\mathcal{S}_{h2}$). Perhaps the best

---

$R < h$, since $\langle \Delta \xi(1, 1/2) \rangle \approx -0.5$, and since 0.5 is 25% of 2 $\approx \langle \zeta(1, 1/2) \rangle$.

[7] If $\sigma^+_{25\%}$ of some quantity X is accurately determined, then the probability of a value of X to be smaller than $\sigma^+_{25\%}(X)$ is 62.5% (i.e., $P(X < \sigma^+_{25\%}(X)) = 0.5 + 0.25/2 = 0.625$).

[8] Since $P(X < \sigma^+_{50\%}(X)) = 0.5 + 0.50/2 = 0.75$.
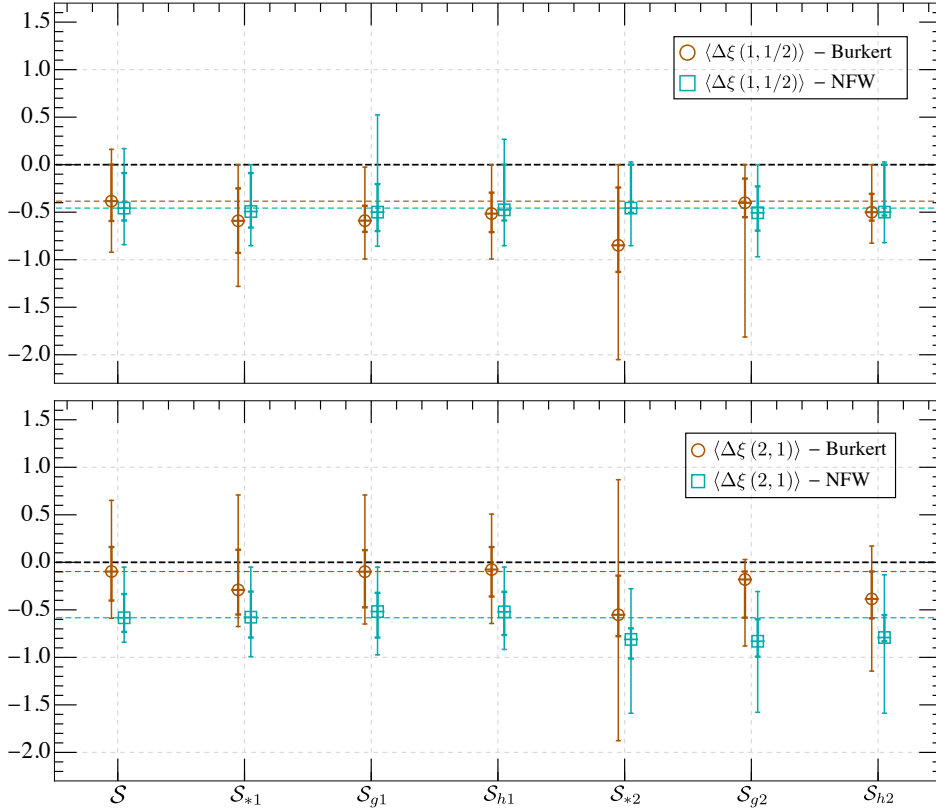
Figure 3. Results for the medians and dispersions of $\Delta\xi(1, 1/2)$ and $\Delta\xi(2, 1)$, considering the complete sample $\mathcal{S}$ and the six subsamples whose definitions can be found in Table 2. The medians are denoted by a circle, for the Burkert profile, and with an open square, for the NFW profile. Each of these medians have two error bars, one, the most interior one, for the dispersion evaluated using $\sigma_{25\%}$, while the other is computed from $\sigma_{50\%}$. The thick black dashed line indicates the expected value of $\langle\Delta\xi\rangle$ for an ideal model whose fits are homogeneous along the galaxy radius, which is zero. The two thinner dashed lines indicate the values of $\langle\Delta\xi\rangle$ computed for the complete $\mathcal{S}$ sample and associated either to the Burkert profile (with brown color), or to the NFW profile (with cyan color). These results are discussed in Secs. 5 and 6.

DM profile is neither one of these two, but clearly the Burkert profile results are better than the NFW results, and this tendency persists even considering only the largest galaxies (i.e., using the subsamples $\mathcal{S}_*$, $\mathcal{S}_g$, $\mathcal{S}_h$). This is one of the main results of this work.

For the subsamples S_*, S_g, and S_h, the Burkert profile results are essentially the same, with a small tendency towards better fitting the region $h < R < 2h$ than the region $R < h$ for the three most stringent subsamples. On the other hand, the NFW profile is clearly worse for these subsamples. The restriction to such large galaxies actually worsens the NFW situation instead of improving it, as it can be seen from Fig. 3 and also, in more detail, from Figs. B1, B2, B3, B4.

6   CONCLUSIONS AND DISCUSSION

Here we use observational data of 62 galaxies fitted with both the NFW profile (whose fits come from Rodrigues et al. 2014) and the Burkert profile (which are new results presented here, see Table 4). We perform four different comparisons between the NFW and Burkert profiles, namely: i) a straightforward test that compares the values of the minimum χ^2 for each galaxy and each profile (Fig. 1, see

also Table 5); ii) correlations between quality of the fits (i.e., minimum χ^2) and global galaxy parameters (stellar mass, disc scale length, final velocity V_f and gas mass, see Fig. 2); iii) evaluations on the homogeneity of the fits along the galaxy radius for the whole sample by using the quantities ξ and ζ that were introduced in Sec. 2, and whose results can be seen in the first plots of Figs. B1 and B3; iv) evaluation of trends on the evolution of homogeneity using different criteria to specify "large" galaxies (Fig. 3 summarizes the results, and the details are given in Appendix B).

Considering the four analyses above, we find that: i) among the 62 galaxies, only 13 are better fitted by the NFW halo profile with respect to the Burkert profile; ii) we found evidence for a trend such that for larger galaxies the NFW profile has a systematic tendency towards improving its fits in comparison with the Burkert one, but it does not fit better than the Burkert profile for $M_* \lesssim 10^{10.5} M_\odot$. The NFW profile may be the best profile for $M_* \gtrsim 10^{11}$, but these are very massive galaxies, and the sample that we use in this work only has a few of them. iii) The homogeneity tests show that the Burkert profile results are consistent with homogeneity (considering the quantity $\Delta\xi(2, 1)$), while the NFW fits have a tendency towards better fitting the region between h and $2h$ than the region between the galaxy centre and h, where h

is the disc scale length. iv) By restricting the galaxy sample to the subsamples that select the largest galaxies according to different criteria, we find that the results on the homogeneity tests with ξ and ζ are essentially the same, and hence the NFW profile still leads to non-homogeneous fits considering only the galaxies with $M_* > 10^9 M_\odot$, or even $M_* > 10^{10} M_*$. Therefore, we confirm the results of Spano et al. (2008) that a cored profile – the Burkert profile in this work – can on average lead to significantly better results than the NFW profile, even for large, very massive, galaxies.[9]

If the DM content of real galaxies follows a universal profile, the above result states that such universal profile should be closer to the Burkert profile than the NFW one. This interpretation is in accordance with the much debated existence of a universal constant dark matter halo surface density (Kormendy & Freeman 2004; Salucci et al. 2007; Donato et al. 2009; Gentile et al. 2009; Kormendy & Freeman 2016), see, however, Del Popolo et al. (2013); Saburova & Del Popolo (2014). On the other hand, it is also important to stress that our results do not imply the existence of a universal DM profile, since there may exist a significative amount of galaxies that evolve naturally towards cuspy DM profiles. For instance, our results are not in conflict with those of Simon et al. (2005).

If the trends that we find here persist once the sample is enlarged, the derived results would be in conflict with certain expectations from the most well known mechanisms able to flatten the DM cusp, namely, supernova feedback and dynamical friction generated by baryonic clumps. They have different predictions for low mass galaxies, like for the dwarf spheroidals (Del Popolo & Le Delliou 2017), but both of them are especially effective at $M_* \sim 10^{8.5} M_\odot$, and both lead to DM halos that are well described by a NFW profile when $M_* \sim 10^{10} M_\odot$. From Fig. 2 it is possible to see that there is a trend such that, for the most massive galaxies, the internal dynamics reduces its strong preference for the cored profile in favour of the cuspy NFW profile, qualitatively as expected from the simulations and the two mechanisms just cited. The problem comes from the details, since a clear preference for the NFW cannot be spotted as even for the galaxies with $M_* > 10^{10} M_\odot$ the data still favour the Burkert profile. For such massive galaxies, these two effects are not expected to be effective on flattening the central profile, hence it may be a sign that an additional baryonic effect is taking place. For instance, for the largest galaxies considered here, AGN feedback is perhaps relevant, and it may be responsible for the DM profile flattening of many of the largest disc galaxies (Peirani et al. 2016) (at cluster scales, see, e.g., Del Popolo 2012c; Martizzi et al. 2013). Another possible interpretation is that the baryonic physics modeling is correct, but the DM physics must be changed (e.g., some kind of self-interacting DM, or modified gravity).

At last, concerning the new technique presented here, we tested the quantities $\xi(2,1)$, $\xi(1, 1/2)$ and related quan-

tities (ζ and $\Delta\xi$). We found that the values of $\langle\xi(2,1)\rangle$ are compatible with homogeneous fits if the Burkert profile is used, while homogeneity is not achieved by using the NFW profile (see Fig. 3). This tension with the NFW profile is not reduced by selecting only the largest galaxies from our sample. For the quantity $\langle\xi(1, 1/2)\rangle$, both the profiles yielded similar results, with both of them being marginally compatible with homogeneous fits. The latter small tension for both profiles either stays the same or increases when considering the largest galaxies. This behaviour suggests the presence of a systematic issue with the stellar profile close to the galaxy centres. Nonetheless, further investigation is necessary to confirm the latter issue, which we plan to do in a future work.

APPENDIX A: DISTRIBUTION OF ξ

To derive the quantity ξ, as defined in eq. (3), one first minimizes the χ^2 relative to the full sample of N points and then takes the ratio of the two pieces of χ^2 with number of data points given by $N(nh)$ and $N(mh)$, respectively, where $1 \leq N(mh) \leq N$ and $1 \leq N(nh) \leq N$.

In order to understand the ξ statistics, we start by assuming that the data are homogeneously distributed and dense enough such that $N(mh)/N(nh) = m/n$. To clarify the analyses we introduce here the following quantity, which is similar to χ_h^2 (see eq. 2),

$$\chi_{mh,nh}^2 \equiv \sum_{i=N(nh)+1}^{N(mh)} \left(\frac{V_{\mathrm{model}}(R_i, \bar{p}_j) - V_i}{\sigma_i} \right)^2, \quad \text{(A1)}$$

so that one can define (with $m > n$),

$$\xi_{\mathrm{ind}}(m, n) \equiv \frac{\chi_{mh,nh}^2}{\chi_{nh}^2} = \xi(m, n) - 1. \quad \text{(A2)}$$

Although its relation to ξ is simple, the quantity ξ_{ind} is useful since it clearly only depends on independent data points. To simplify the analysis, we assume that $N(nh) \gg N_p$, where N_p is the number of parameters p_j. Then, one sees from eq. (A2) that ξ_{ind} is distributed according to a scaled F-distribution with $\{N(mh) - N(nh), N(nh)\}$ degrees of freedom. Consequently, its median and its mean can be derived as follows

$$\langle\xi_{\mathrm{ind}}(kn, n)\rangle = \frac{1}{I_{\left(1, -\frac{1}{2}\right)}^{-1}\left(\frac{N(nh)}{2}, (k-1)\frac{N(nh)}{2}\right)} - 1, \quad \text{(A3)}$$

$$\overline{\xi_{\mathrm{ind}}(kn, n)} = (k-1)\frac{N(nh)}{N(nh) - 2}, \quad \text{(A4)}$$

---

[9] On the other hand, there is the possibility that an important aspect of baryonic physics is not being properly modeled by the observational data analysis. If this is the case, then the results relative to the largest galaxies are more prone to significative changes than the results relative to the smaller ones.
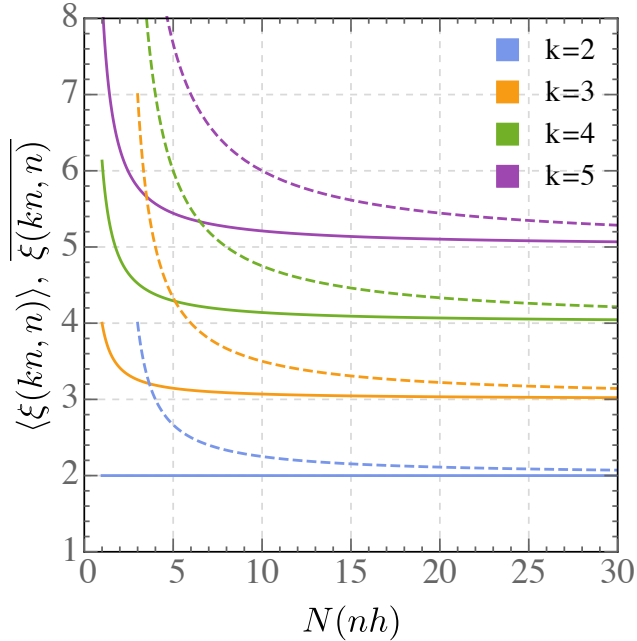
Figure A1. The median (solid line, plotted for $N(nh) \geq 1$) and the mean (dashed line, plotted for $N(nh) \geq 3$)) of $\xi(kn, n)$ as functions of $N(nh)$. From the plot above, the mean shows a much slower convergence than the median. The case $k = 2$ is a special case, it is the only case in which the median is independent of $N(nh)$ (within the assumptions of this appendix). All the ξ quantities computed from galaxies data in this paper use $k = 2$, and the plot above motivates this choice.

where we used kn in place of m, $\langle \ \rangle$ denotes the median, a bar over a quantity denotes its mean value, the result for the mean is valid for $N(nh) \geq 3$, and I^{-1} is the inverse of the generalized regularized incomplete beta function.[10] For $N(nh)$ sufficiently large, one finds that $\langle \xi_{\mathrm{ind}} \rangle \approx \bar{\xi}_{\mathrm{ind}} \approx k - 1$, which is equivalent to eq. (4).

For the particular case $k = 2$, changing the variable back to ξ, in place of ξ_{ind}, we find,

$$\langle \xi(2n, n) \rangle = 2 \,, \tag{A5}$$

$$\overline{\xi(2n, n)} = 2 \, \frac{N(nh) - 1}{N(nh) - 2} \,. \tag{A6}$$

This shows that – within the assumption of this section – eq. (4) holds exactly if the average is the median and if $m = 2n$. For other values of m and n, the same equation still holds, but under an additional approximation.

Besides the important issue with outliers, commented in Sec. 2, the median has an additional convenience, since the convergence of the median of the F-distribution to the value given by eq. (4) is much faster than the convergence of the mean. This can be seen in Fig. A1.

The main purpose of this appendix is to further clarify and motivate the use of $\xi(2n, n)$ and related quantities that we used in this paper. Some assumptions used in this appendix were evoked for simplicity and are too restrictive

---

[10] That is, $I_{(z_0, z_1)}(a, b) = B(z_0, z_1, a, b)/B(a, b)$, where $B(a, b)$ is the beta function and $B(z_0, z_1, a, b) \equiv \int_{z_0}^{z_1} t^{a-1}(1 - t)^{b-1} dt$ is the generalized incomplete beta function.

---

considering the data that we use here. Further analyses, either with more data from galaxies, or theoretical developments on the statistics will be purpose of a future work.

In Sec. 2 we agued in favour of the existence of some kind of average that would be compatible with eq. (4), and also be compatible with the type of data that we deal with galaxies, namely data with a significative number of outliers. The above results confirm that the median is suited for describing the average (4), and favour the use of $k = 2$.

APPENDIX B: PLOTS OF ξ, ζ AND $\Delta\xi$

Here we show in detail the plots of ξ, ζ and $\Delta\xi$ for all the subsamples considered in this work. These plots are in Figs. B1, B3, B2 and B4.

APPENDIX C: THE EXPECTED AND THE DERIVED STELLAR MASS-TO-LIGHT RATIOS

In this work, the stellar mass-to-light ratios (Υ_*) were all derived from best fits from RC data. In this appendix we compare the derived values with the expected ones, and evaluate the consequences of changes on Υ_* for the results on ξ and related quantities.

In general, by comparing best fits that consider different dark matter profiles and use Υ_* as a free parameter, one is testing the total combination of dark matter and the stellar component(s). If the derived values of Υ_* are systematically reasonable for one of the dark matter models, but not for the other, this alone would be an evidence in favour of the first model. In this case there would be a tension between the values of Υ_* that this model favours and the values of Υ_* that are expected to be physically viable (from stellar population synthesis models, dynamical arguments, or scaling laws like the Baryonic Tully-Fisher relation). If both the dark matter models lead to reasonable values of Υ_*, then the comparison between the best fits results of each of the models is a comparison between these models.

The stellar components of the samples A and B are determined from infrared observations (with 3.6 μm wave length for Sample A and I-band for the Sample B). These samples include most of the massive and luminous large galaxies that are considered in this work. Besides estimating values of Υ_* from stellar population synthesis models, the corresponding references agree that there is significant uncertainty on Υ_*, in part due to uncertainties on the stellar initial mass function (IMF), leading to uncertainties on Υ_* of about a factor two. Hence, as one of their approaches, the Υ_* values are derived from best fit procedures. de Blok et al. (2008) show that for some galaxies the expected value of Υ_* leads to a reasonable dynamical picture, and the fitted values of Υ_* also agree with the latter; but there are also examples of some galaxies that show tensions between the expected and the fitted values. It was found that the NFW profile favours the Kroupa IMF, while other profiles may favour different IMF's.

Based on results from stellar population synthesis models (McGaugh & Schombert 2014; Meidt et al. 2014; Schombert & McGaugh 2014) and, also, on the minimization of the baryonic Tully-Fisher relation (BTFR) dispersion
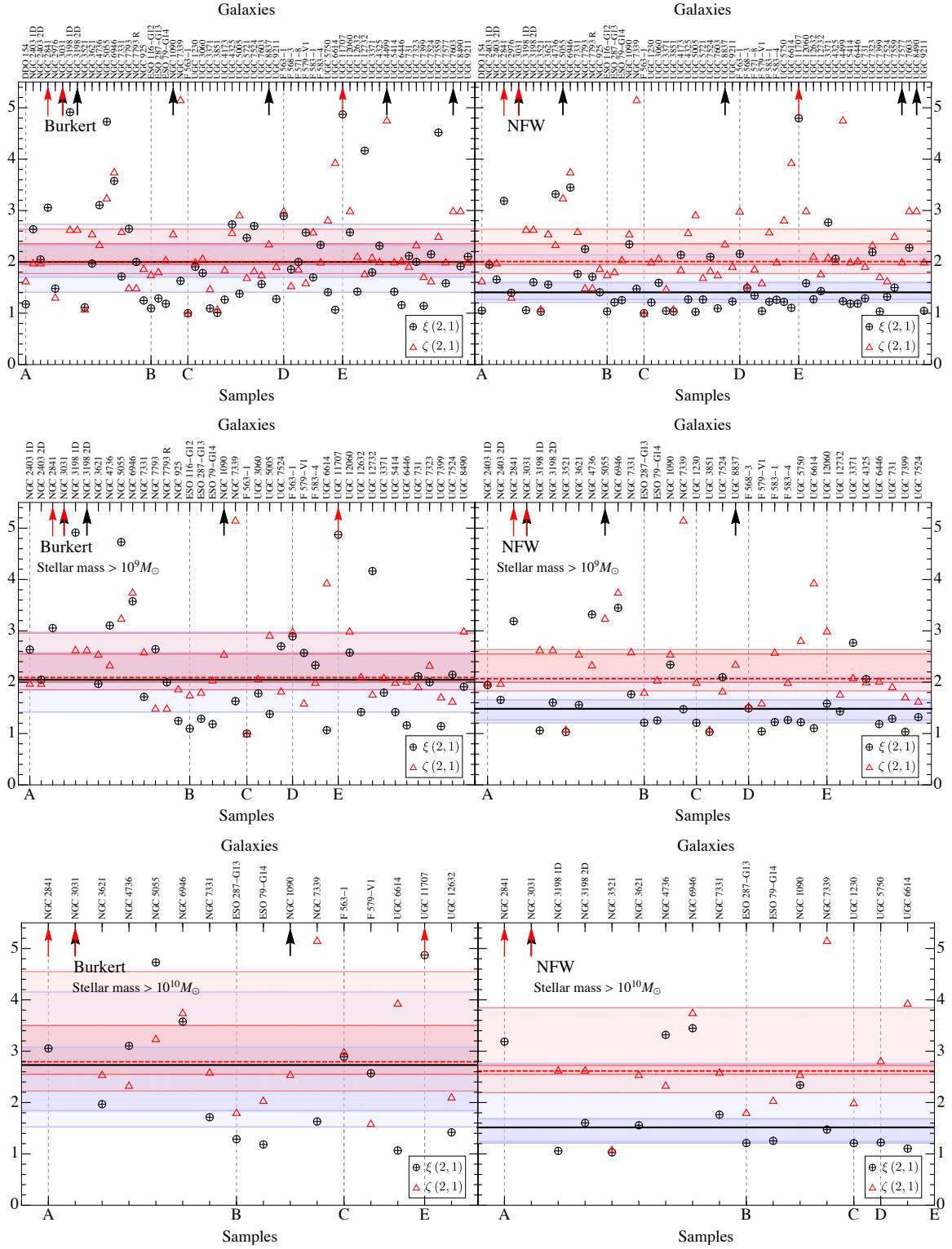
Figure B1. Plots that show the values of $\xi(2,1), \zeta(2,1)$, their medians and their dispersions. The dashed red and the solid black lines show respectively the values of $\langle \zeta(2,1) \rangle$ and $\langle \xi(2,1) \rangle$. The lighter and darker red regions are respectively the regions between $\sigma^-_{50\%}(\zeta(2,1))$ and $\sigma^+_{50\%}(\zeta(2,1))$, and between $\sigma^-_{25\%}(\zeta(2,1))$ and $\sigma^+_{25\%}(\zeta(2,1))$. The darker and lighter blue regions follow analogously, but for $\xi(2,1)$. The two plots in the first line refer to the total sample $\mathcal{S}$, and those in the second and third lines refer respectively to the samples $\mathcal{S}_{*1}$ and $\mathcal{S}_{*2}$. The arrows indicate data whose corresponding values are outside the plotted region. The plots above show that $\langle \xi(2,1) \rangle \approx \langle \zeta(2,1) \rangle$ for the Burkert fits, while $\langle \xi(2,1) \rangle < \langle \zeta(2,1) \rangle$ for the NFW fits.
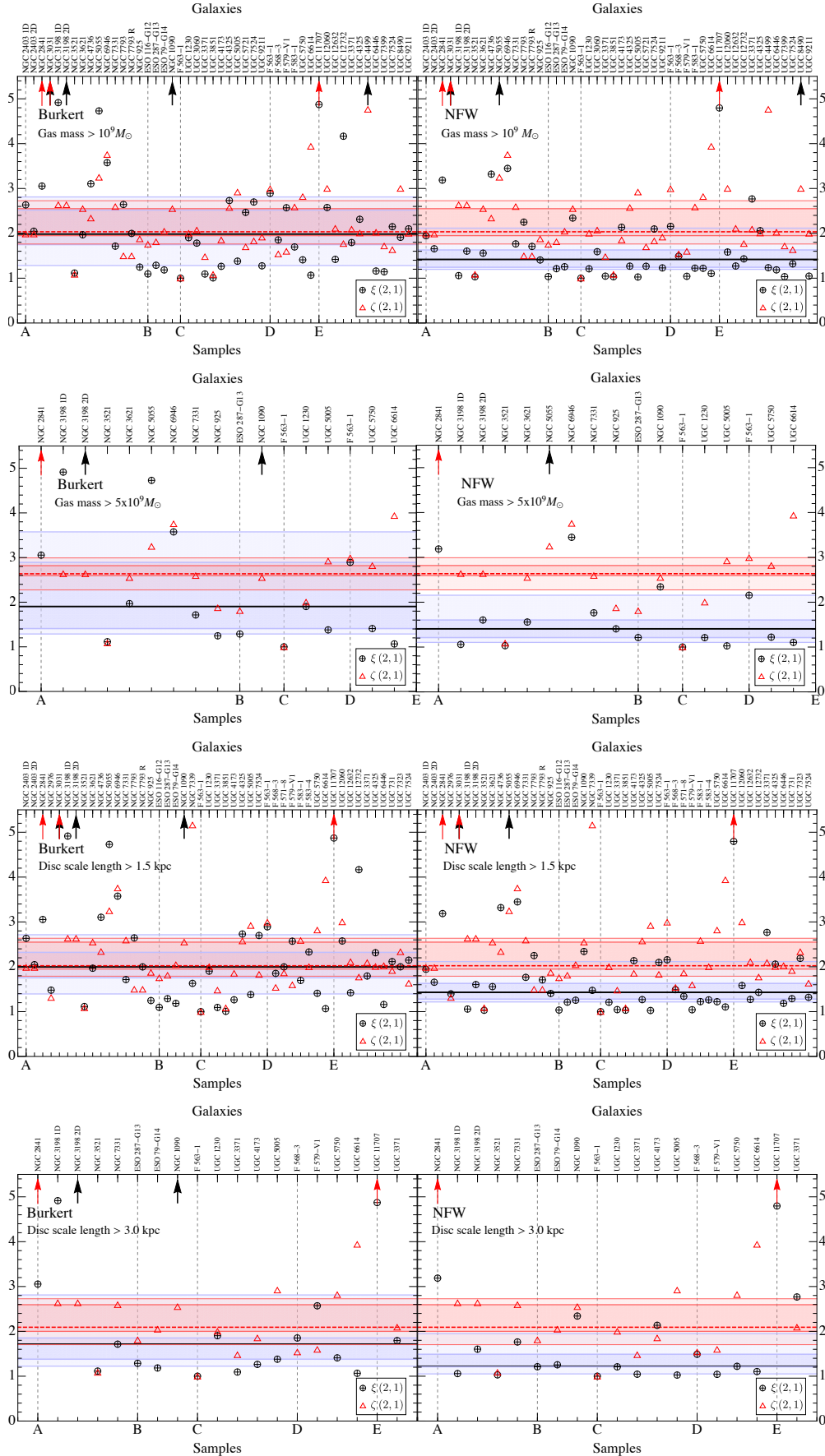
Figure B2. These plots show the values of $\xi(2,1), \zeta(2,1)$, their medians and their dispersions. The symbols follow the same conventions of Fig. B1. From top to bottom, the subsample relative to a given row is, respectively, $\mathcal{S}_{g1}$, $\mathcal{S}_{g2}$, $\mathcal{S}_{h1}$ and $\mathcal{S}_{h2}$.
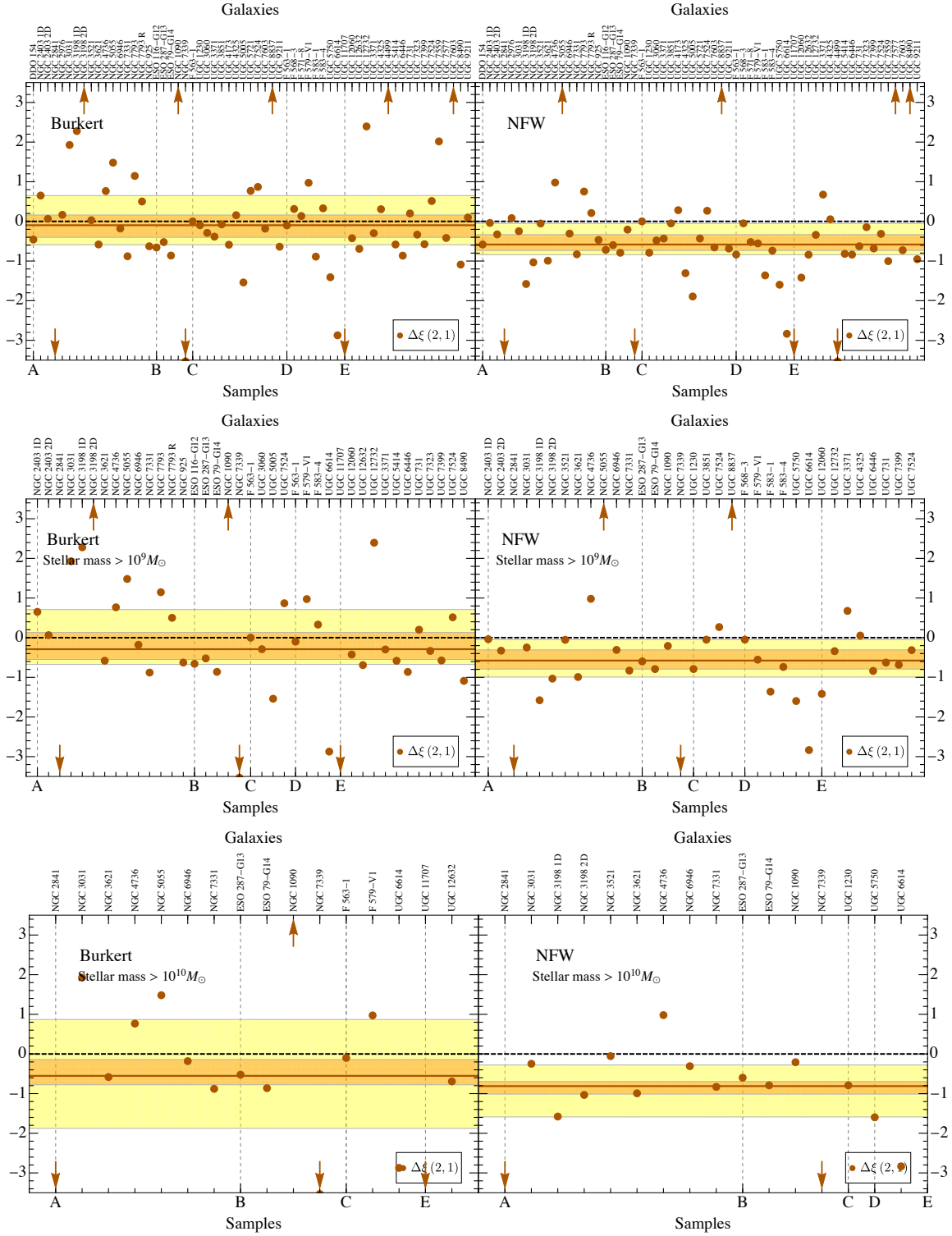
Figure B3. Plots that show the values of $\Delta\xi(2,1)$, its median and dispersion. The solid brown and the dashed black lines show respectively the value of $\langle\Delta\xi(2,1)\rangle$ and its expected value, i.e. zero. The lighter and darker yellow regions are the dispersions derived from $\sigma_{50\%}^{\pm}(\Delta\xi(2,1))$ and $\sigma_{25\%}^{\pm}(\Delta\xi(2,1))$ respectively. See also Fig. B1. These plots are consistent with $\langle\Delta\xi(2,1)\rangle \approx 0$ (i.e., homogeneous fit) for the Burkert profile and $\langle\Delta\xi(2,1)\rangle < 0$ for the NFW profile.
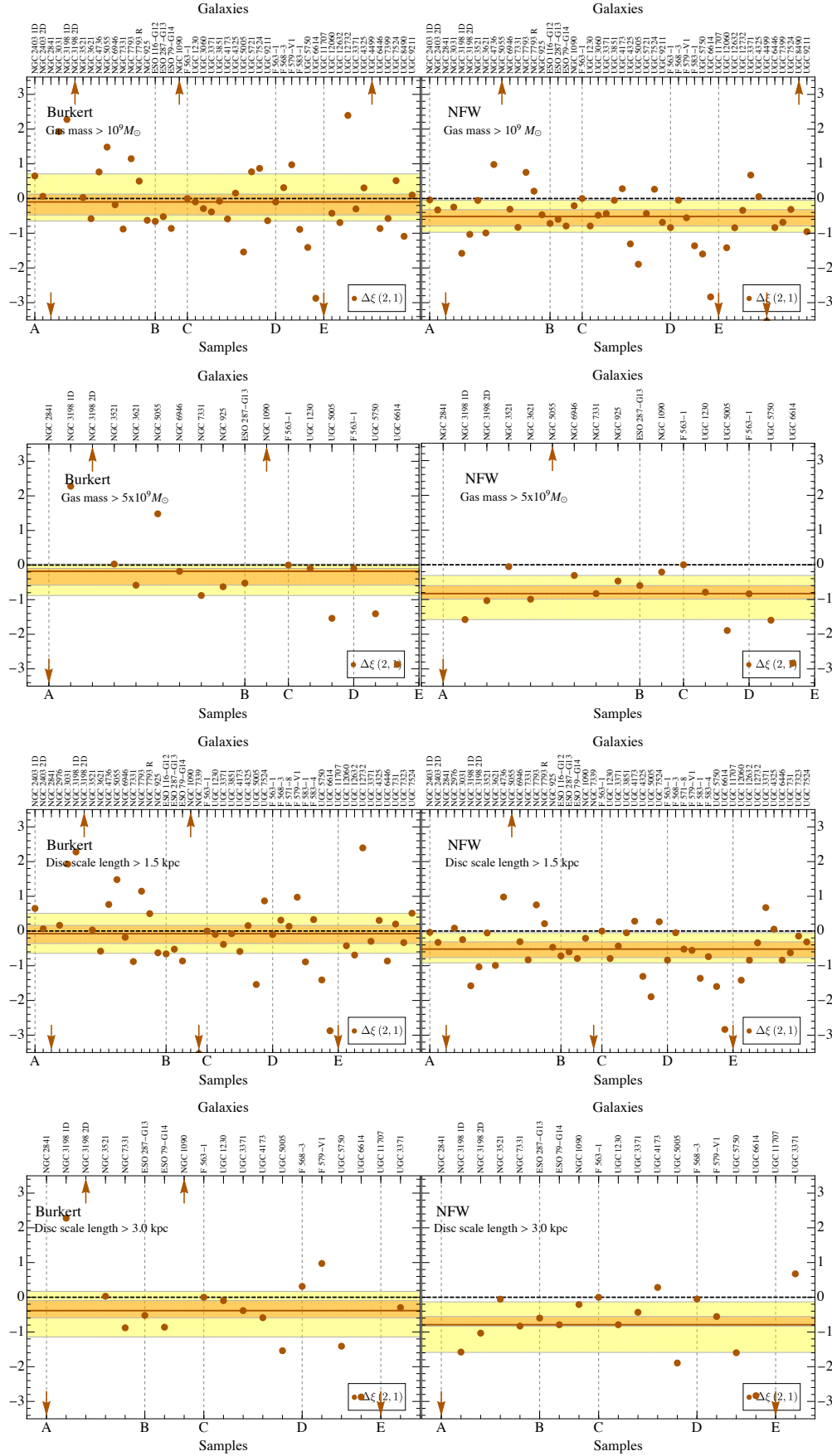
Figure B4. These plots show the values of $\Delta\xi(2,1)$, its median and dispersion. The symbols follow the same conventions of Fig. B3. From top to bottom, the subsample relative to a given row is, respectively, $\mathcal{S}_{g1}$, $\mathcal{S}_{g2}$, $\mathcal{S}_{h1}$ and $\mathcal{S}_{h2}$.
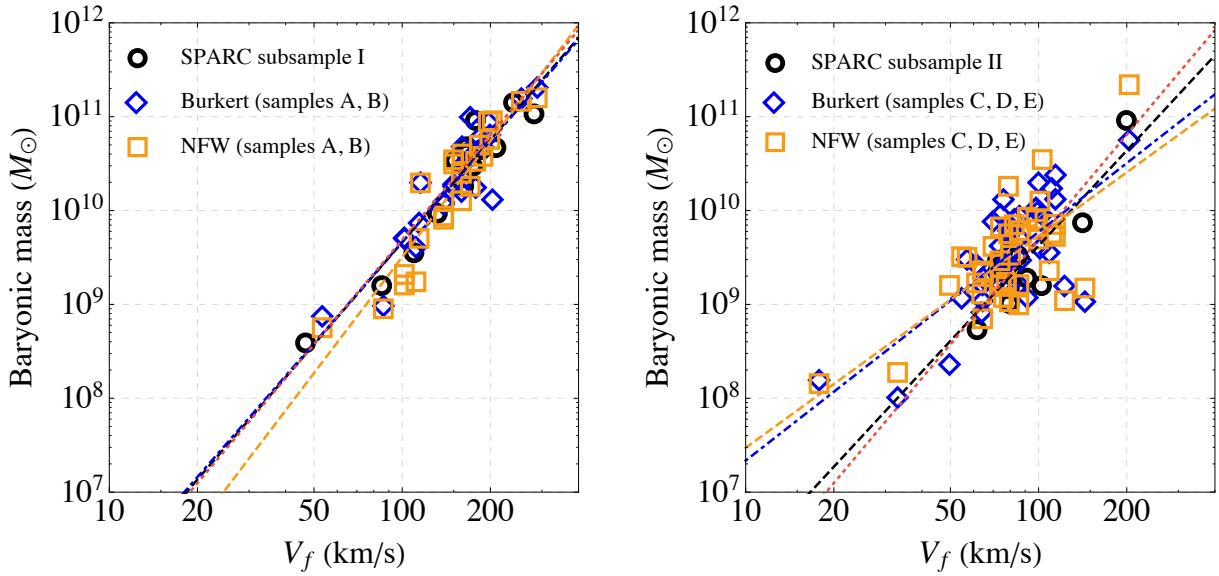
Figure C1. A comparison between the best fit Υ_*, for the NFW and the Burkert profiles, and the BTFR. The left plot considers only the data from the samples A and B, and the data from SPARC that correspond to the same galaxies (subsample I). The right plot considers the samples C, D and E, together with the data from SPARC that correspond to the same galaxies (subsample II). The red dotted line shows the BTFR law from Lelli et al. (2016b), the dashed black line is the BTFR result considering only the SPARC data that appears in each of the plots above. The dot-dashed blue and the dashed orange lines show the best straight lines that describe the BTFR inferred from the Burkert or the NFW halo respectively. There is good agreement between the SPARC data and the derived values of Υ_* in this work for the Samples A and B, while for Samples C, D and E the dispersion is too large to infer the BTFR from the fitted values of Υ_*.

(Lelli et al. 2016b), Lelli et al. (2016a) consider the simplifying hypothesis that[11] $\Upsilon_* = 0.5$ for all the stellar discs at 3.6 μm. Although the use of $\Upsilon_* = 0.5$ is too restrictive to be true for all galaxies, at least it is a reasonable starting point to study general properties of galaxies. Therefore, we compare our results on the inferred Υ_* values with those of the SPARC sample (Lelli et al. 2016a).

Some of the galaxies that constitute the SPARC sample can also be found in the samples A and B, and we use these, together with the complete SPARC results on the BTFR, in order to check our results on Υ_*. We will call "SPARC subsample I" the collection of the latter SPARC galaxies. These comparisons are performed in Fig. C1. It can be seen that both the NFW and the Burkert fits lead to BTFRs that are very close to that found from SPARC.

Writing M_b for the baryonic mass and V_f for the final circular velocity the BTFR has the form,

$$\log_{10} M_b = a \log_{10} V_f + b. \qquad (C1)$$

To be clear, the baryonic mass M_b is defined as the total mass of gas (hydrogen and helium) plus the mass from the stellar components of each galaxy. V_f is essentially the observed circular velocity that is farthest from the galaxy center, and this is the definition used to generate the plots in Fig. C1 for the NFW and Burkert data. Lelli et al. (2016b) use a more robust variation for the definition for V_f, which in the end leads to small changes that are not relevant to the purposes of this appendix. This difference on the V_f, together with small differences on the RC data itself, is the reason that the SPARC data that appear in Fig. C1 is slightly displaced in the V_f axis for some galaxies.

The best fit values for a and b read,:

$$a = 3.71, \; b = 2.27 \quad : \text{full SPARC sample}$$
$$a = 3.62, \; b = 2.43 \quad : \text{SPARC subsample I}$$
$$a = 3.58, \; b = 2.50 \quad : \text{Burkert for Samples A and B}$$
$$a = 4.11, \; b = 1.29 \quad : \text{NFW for Samples A and B.}$$

Although differences can promptly be seen in the numbers above, in the range $20 < V_f/(\text{km/s}) < 300$ the corresponding lines are very close (see the left plot in Fig. C1), with three of them being almost indistinguishable.

The situation with the stellar components of the samples C, D and E is clearly different. These samples are dominated by dwarf and LSB galaxies. These galaxies have observed RCs and stellar components that allow for large variations on Υ_*.[12] The right hand side plot in Fig. C1 shows a large dispersion on Υ_* for a given value of V_f. By considering the error bars on Υ_* derived from the fits, which are not small for these galaxies, the compatibility with the BTFR dispersion is improved.

For the case of the Samples C, D, and E, the best fit

---

[11] See, however, Angus et al. (2016); Papastergis et al. (2016).

[12] This claim is supported by Swaters et al. (2011), and in particular by Lelli et al. (2016a). According to the latter, for the large luminous galaxies, $\Upsilon_* = 0.5$ at [3.6] leads to stellar RCs close to maximal, while for the LSB and dwarfs with that same value for Υ_* much lower relative stellar contributions are found, such that dark matter commonly dominates at $2.2\,h$, (i.e., at the maximum of the stellar disc contribution to the RC).

for the BTFR parameters is not particularly meaningful, and does not show a robust systematic deviation from the standard BTFR, since the corresponding error on the a and b parameters (see eq. C1) is large. The distribution of the data in the plane $M_b \times V_f$ is essentially the same for both of the models, hence the large dispersion on Υ_* does not introduce a bias in favour of any one of the models.

It should be verified whether the large dispersion in Υ_* for the samples C, D, and E has impact on the results relative to the quantity ξ. Considering the figures on the ξ and ζ results, Figs. B1, B2, the large dispersion on Υ_* could at most increase the dispersion on the results of ξ, but without any effect on ζ, since ζ only depends on the observational RC data. The dispersion of the ξ data does not show any clear systematic increase between samples A and B and the samples C, D, and E. The same happens for Figs. B3, B4, where the dispersion on the $\Delta\xi$ data is essentially the same along the samples for a given model. Moreover, although most of the galaxies belong to the samples C, D and E, when considering the subsamples that select the most massive or large galaxies, the relative importance of the samples A and B is increased. Thus, our main results that concern the largest galaxies are specially robust to this issue.

It would be interesting to analyse the data from the SPARC sample using the new methods here proposed, and considering different hypothesis on Υ_*, which we plan to do in a future work.

REFERENCES

Ade P. A. R., et al., 2016, Astron. Astrophys., 594, A13
Angus G. W., Gentile G., Famaey B., 2016, A&A, 585, A17
Begeman K. G., Broeils A. H., Sanders R. H., 1991, MNRAS, 249, 523
Blais-Ouellette S., Amram P., Carignan C., 2001, AJ, 121, 1952
Bode P., Ostriker J. P., Turok N., 2001, ApJ, 556, 93
Borriello A., Salucci P., 2001, MNRAS, 323, 285
Burkert A., 1995, ApJ, 447, L25
Courteau S., et al., 2014, Rev. Mod. Phys., 86, 47
Das S., et al., 2011, Physical Review Letters, 107, 021301
Del Popolo A., 2009, ApJ, 698, 2093
Del Popolo A., 2010, MNRAS, 408, 1808
Del Popolo A., 2011, JCAP, 1107, 014
Del Popolo A., 2012a, MNRAS, 419, 971
Del Popolo A., 2012b, MNRAS, 424, 38
Del Popolo A., 2012c, MNRAS, 424, 38
Del Popolo A., 2013, AIP Conf. Proc., 1548, 2
Del Popolo A., 2014, Int. J. Mod. Phys., D23, 1430005
Del Popolo A., Hiotelis N., 2014, JCAP, 1401, 047
Del Popolo A., Le Delliou M., 2017, Galaxies, 5, 17
Del Popolo A., Pace F., 2016, Astrophys. Space Sci., 361, 162
Del Popolo A., Cardone V. F., Belvedere G., 2013, MNRAS, 429, 1080
Del Popolo A., Lima J., Fabris J. C., Rodrigues D. C., 2014, JCAP, 1404, 021
Di Cintio A., Brook C. B., Macciò A. V., Stinson G. S., Knebe A., Dutton A. A., Wadsley J., 2014, MNRAS, 437, 415
Donato F., et al., 2009, MNRAS, 397, 1169
Famaey B., McGaugh S., 2012, Living Rev. Rel., 15, 10
Flores R. A., Primack J. R., 1994, ApJ, 427, L1
Gao L., Navarro J. F., Cole S., Frenk C., White S. D. M., Springel V., Jenkins A., Neto A. F., 2008, MNRAS, 387, 536
Gentile G., Salucci P., Klein U., Vergani D., Kalberla P., 2004, MNRAS, 351, 903
Gentile G., Burkert A., Salucci P., Klein U., Walter F., 2005, ApJ, 634, L145
Gentile G., Salucci P., Klein U., Granato G. L., 2007, MNRAS, 375, 199
Gentile G., Famaey B., Zhao H., Salucci P., 2009, Nature, 461, 627
Gentile G., Famaey B., de Blok W., 2011, A&A, 527, A76
Gilmore G., Wilkinson M. I., Wyse R. F. G., Kleyna J. T., Koch A., Evans N. W., Grebel E. K., 2007, ApJ, 663, 948
Governato F., et al., 2010, Nature, 463, 203
Governato F., Zolotov A., Pontzen A., Christensen C., Oh S., et al., 2012, MNRAS, 422, 1231
Hand N., et al., 2012, Physical Review Letters, 109, 041101
Hinshaw G., et al., 2013, Astrophys. J. Suppl., 208, 19
Inoue S., Saitoh T. R., 2011, MNRAS, 418, 2527
Karukes E. V., Salucci P., 2017, MNRAS, 465, 4703
Kormendy J., Freeman K. C., 2004, in Ryder S., Pisano D., Walker M., Freeman K., eds, IAU Symposium Vol. 220, Dark Matter in Galaxies. p. 377 (arXiv:astro-ph/0407321)
Kormendy J., Freeman K. C., 2016, ApJ, 817, 84
Lelli F., McGaugh S. S., Schombert J. M., 2016a, AJ, 152, 157
Lelli F., McGaugh S. S., Schombert J. M., 2016b, ApJ, 816, L14
Macciò A. V., Dutton A. A., Bosch F. C. v. d., 2008, MNRAS, 391, 1940
Macciò A. V., Ruchayskiy O., Boyarsky A., Muñoz-Cuartas J. C., 2013, MNRAS, 428, 882
Martizzi D., Teyssier R., Moore B., 2013, MNRAS, 432, 1947
McGaugh S. S., Schombert J. M., 2014, AJ, 148, 77
Meidt S. E., et al., 2014, ApJ, 788, 144
Mo H., van den Bosch F., White S., 2010, Galaxy Formation and Evolution. Cambridge University Press
Moore B., 1994, Nature, 370, 629
Moster B. P., Naab T., White S. D. M., 2013, MNRAS, 428, 3121
Navarro J. F., Eke V. R., Frenk C. S., 1996a, MNRAS, 283, L72
Navarro J. F., Frenk C. S., White S. D. M., 1996b, ApJ, 462, 563
Navarro J. F., Frenk C. S., White S. D., 1997, ApJ, 490, 493
Navarro J. F., et al., 2010, MNRAS, 402, 21
Oh S.-H., Brook C., Governato F., Brinks E., Mayer L., de Blok W. J. G., Brooks A., Walter F., 2011, AJ, 142, 24
Oman K. A., et al., 2015, Mon. Not. Roy. Astron. Soc., 452, 3650
Oman K. A., Navarro J. F., Sales L. V., Fattahi A., Frenk C. S., Sawala T., Schaller M., White S. D. M., 2016, MNRAS, 460, 3610
Oñorbe J., Boylan-Kolchin M., Bullock J. S., Hopkins P. F., Kereš D., Faucher-Giguère C.-A., Quataert E., Murray N., 2015, MNRAS, 454, 2092
Papastergis E., Adams E. A. K., van der Hulst J. M., 2016, A&A, 593, A39
Pawlowski M. S., Famaey B., Merritt D., Kroupa P., 2015, ApJ, 815, 19
Peirani S., et al., 2016, preprint, (arXiv:1611.09922)
Pontzen A., Governato F., 2012, MNRAS, 421, 3464
Primack J. R., 2009, New Journal of Physics, 11
Ricotti M., 2003, MNRAS, 344, 1237
Ricotti M., Pontzen A., Viel M., 2007, ApJ, 663, L53
Rocha M., Peter A. H. G., Bullock J. S., Kaplinghat M., Garrison-Kimmel S., Onorbe J., Moustakas L. A., 2013, MNRAS, 430, 81
Rodrigues D. C., Letelier P. S., Shapiro I. L., 2010, JCAP, 1004, 020
Rodrigues D. C., de Oliveira P. L., Fabris J. C., Gentile G., 2014, MNRAS, 445, 3823
Saburova A., Del Popolo A., 2014, MNRAS, 445, 3512
Salucci P., Lapi A., Tonini C., Gentile G., Yegorova I., Klein U., 2007, MNRAS, 378, 41
Sánchez-Salcedo F. J., Martínez-Gómez E., Aguirre-Torres V. M., Hernández-Toledo H. M., 2016a, MNRAS, 462, 3918

Sanchez-Salcedo F. J., Martinez-Gomez E., Aguirre-Torres V. M., Hernandez-Toledo H. M., 2016b, MNRAS, 462, 3918

Schombert J., McGaugh S., 2014, Publ. Astron. Soc. Australia, 31, e036

Simon J. D., Bolatto A. D., Leroy A., Blitz L., Gates E. L., 2005, ApJ, 621, 757

Spano M., Marcelin M., Amram P., Carignan C., Epinat B., Hernandez O., 2008, MNRAS, 383, 297

Spergel D. N., Steinhardt P. J., 2000, Phys. Rev. Lett., 84, 3760

Stadel J., Potter D., Moore B., Diemand J., Madau P., Zemp M., Kuhlen M., Quilis V., 2009, MNRAS, 398, L21

Swaters R., Madore B., Bosch F. V. D., Balcells M., 2003, ApJ, 583, 732

Swaters R. A., Sancisi R., van Albada T. S., van der Hulst J. M., 2009, A&A, 493, 871

Swaters R., Sancisi R., van Albada T., van der Hulst J., 2011, ApJ, 729, 118

Taylor J. E., Navarro J. F., 2001, ApJ, 563, 483

Tollet E., et al., 2016, MNRAS, 456, 3542

Walter F., Brinks E., de Blok W. J. G., Bigiel F., Kennicutt Jr. R. C., Thornley M. D., Leroy A., 2008, AJ, 136, 2563

Weinberg D. H., Bullock J. S., Governato F., de Naray R. K., Peter A. H. G., 2013, in Sackler Colloquium: Dark Matter Universe: On the Threshhold of Discovery Irvine, USA, October 18-20, 2012. (arXiv:1306.0913), http://inspirehep.net/record/1237028/files/arXiv:1306.0913.pdf

Zentner A. R., Bullock J. S., 2003, ApJ, 598, 49

Zlosnik T. G., Ferreira P. G., Starkman G. D., 2007, Phys. Rev., D75, 044017

de Almeida Á. O. F., Piattella O. F., Rodrigues D. C., 2016, MNRAS, 462, 2706

de Blok W., 2010, Adv.Astron., 2010, 789293

de Blok W., Bosma A., 2002, A&A, 385, 816

de Blok W. J. G., McGaugh S. S., Rubin V. C., 2001a, AJ, 122, 2396

de Blok W., McGaugh S. S., Bosma A., Rubin V. C., 2001b, ApJ, 552, L23

de Blok W. J. G., Walter F., Brinks E., Trachternach C., Oh S., Kennicutt R. C., 2008, AJ, 136, 2648

de Souza R. S., Rodrigues L. F. S., Ishida E. E., Opher R., 2011, MNRAS, 415, 2969

van den Bosch F. C., Dalcanton J. J., 2000, ApJ, 534, 146

This paper has been typeset from a TeX/LaTeX file prepared by the author.